Petroleum Science 23 (2026) 4810–4828

Contents lists available at ScienceDirect

Petroleum Science

journal homepage: www.keaipublishing.com/en/journals/petroleum-science

Original Paper

Fully anisotropic undrained effects on short-term wellbore stability of arbitrarily inclined wells in transversely isotropic formations

Wen-Da Li [a], Ya-Yun Zhang [b], Ming-Ming Zhang [b], Yan Jin [c,d,*], Yun-Hu Lu [c,d], Yang Xia [c,d], Shi-Ming Wei [c]

[a] Key Laboratory of In-situ Property-improving Mining of Ministry of Education, Taiyuan University of Technology, Taiyuan, 030024, Shanxi, China
[b] State Key Laboratory of Shale Oil and Gas Enrichment Mechanisms and Effective Development, Beijing, 102206, China
[c] State Key Laboratory of Petroleum Resources and Engineering, China University of Petroleum (Beijing), Beijing, 102249, China
[d] College of Petroleum Engineering, China University of Petroleum(Beijing), Beijing, 102249, China

ARTICLE INFO

Article history:
Received 23 February 2026
Received in revised form
15 April 2026
Accepted 21 June 2026
Available online 24 June 2026

Edited by Jia-Jia Fei

Keywords:
Wellbore stability
Undrained stress solution
Undrained pore pressure response
Collapse pressure
Anisotropic poroelastic effect

ABSTRACT

The immediate undrained poroelastic response after drilling is critical for short-term wellbore stability in low-permeability formations. Despite its significance, existing analytical undrained wellbore stress solutions in transversely isotropic formations are limited to special cases where the borehole axis is either perpendicular or parallel to the plane of transverse isotropy. By extending Amadei's elastic framework into the undrained poroelastic regime, this study presents an analytical undrained solution for arbitrarily inclined boreholes in transversely isotropic formations, considering fully anisotropic undrained poroelastic effects. Validation against undrained isotropic and transversely isotropic solutions, as well as anisotropic Biot's effective stress coefficients, demonstrates the robustness of the proposed model. The derived Biot's effective stresses are subsequently applied to evaluate short-term collapse pressure with varying wellbore trajectories. Results show that undrained wellbore stress distributions deviate significantly from drained Amadei solution with varying elastic property anisotropy and wellbore pressure, particularly in terms of axial and shear stress components. Furthermore, estimating the undrained pore pressure response using drained Amadei stress solution introduces substantial errors, highlighting the necessity of adopting a fully anisotropic undrained poroelastic framework. Unlike isotropic formations, the anisotropic undrained pore pressure response exhibits an asymmetrical distribution, reflecting coupled shear-tension and solid-fluid couplings. Polar plots of collapse pressure that incorporate the undrained effect exhibit significant differences compared to those derived from previous models, indicating that the optimal drilling direction may not coincide with the orientation of the horizontal principal stress. This analytical solution establishes a benchmark for fully anisotropic undrained wellbore stress distribution and holds substantial implications for enhancing early-stage wellbore stability assessments in strongly anisotropic poroelastic formations.

1. Introduction

Poroelasticity, as established by Biot (1941) and further developed by Rice and Cleary (1976), is a critical framework for analyzing borehole stability within porous geological formations (Detournay and Cheng, 1988). Existing analytical poroelastic models predominantly assume isotropic material properties or consider special wellbore trajectories perpendicular or parallel to the transversely isotropic plane (Cui et al., 1998; Abousleiman and Cui, 1998; Abousleiman and Ekbote, 2005; Kanj and Abousleiman, 2005; Bobet, 2011; Liu et al., 2015; Gao et al., 2017; Cheng et al., 2019; Gao and Chen, 2020; Tran et al., 2022; Chen et al., 2023; Fan et al., 2025; Lu et al., 2025). For arbitrarily inclined wells in transversely isotropic formations, analyses often rely on purely elastic anisotropic solutions that inherently exclude poroelastic effects (Lekhnitskii, 1963; Amadei, 1983; Aadnoy, 1989; Fang, 2018; Wang et al., 2022). However, these purely elastic analytical models are inadequate for accurately simulating conditions such as drilling in porous formations, as they overlook the critical influence of pore pressure variations (Fjar et al., 2008).

* Corresponding author.
E-mail address: jiny@cup.edu.cn (Y. Jin).
Peer review under the responsibility of China University of Petroleum (Beijing).

https://doi.org/10.1016/j.petsci.2026.06.037
1995-8226/

List of symbols

σ_h, σ_H, σ_v	In-situ stress components under PCS
$\varepsilon_x, \varepsilon_y, \varepsilon_z, \varepsilon_{yz}, \varepsilon_{xz}, \varepsilon_{xy}$	Normal and shear strains
$\sigma_{rr}, \sigma_{\theta\theta}, \sigma_{zz}, \tau_{r\theta}, \tau_{rz}, \tau_{\theta z}$	Stress components on the borehole wall
$S_i^{\text{eff}}(i = 1-3)$	Biot's effective principal stresses
p_0, p	Initial and present pore pressure, respectively
α_b, β_b	Wellbore azimuth and inclination angle, respectively
$\boldsymbol{D}$, $\boldsymbol{A}$	Stiffness and compliance constitutive matrix, respectively
M	Biot modulus
φ	Porosity
ν, ν'	Horizontal and vertical Poisson's ratio
$\boldsymbol{N}$, $\boldsymbol{T}$	Bond transformation matrices
$\boldsymbol{A}_t$, $\boldsymbol{\alpha}_t$	Compliance and Biot's effective stress coefficients matrices under BCS, respectively
μ_1, μ_2, μ_3	Characteristic roots
i	Imaginary unit
c, ϕ	Cohesion and friction angle of matrix
a, b	Mogi-Collomb coefficients related to c and ϕ
F	Shear failure potential
$\sigma_x, \sigma_y, \sigma_z, \tau_{yz}, \tau_{xz}, \tau_{xy}$	Total normal and shear stresses
$\sigma_{xx}^b, \sigma_{yy}^b, \sigma_{zz}^b, \tau_{yz}^b, \tau_{xz}^b, \tau_{xy}^b$	Far-field stress components under BCS
S_i (i = 1–3)	Principal stresses under BCS
P_w	Wellbore pressure
α_s, β_s	Offset angles of maximum horizontal and vertical stresses under PCS, respectively
$\alpha_{bp}+\pi$, β_{bp}	Dip direction and angle of BP, respectively
α_h, α_v	Horizontal and vertical Biot's effective stress coefficients under BPCS, respectively
ζ	Fluid content variation per unit volume
K^*	Bulk modulus
$\boldsymbol{R}_1$, $\boldsymbol{R}_2$, $\boldsymbol{R}_3$	Transformation matrices
E, E'	Horizontal and vertical elastic modulus under BPCS, respectively
K_s, K_f	Modulus of solid grain and fluid
Δp	Induced undrained pore pressure
c_w, ϕ_w	Cohesion and friction angle of matrix, respectively
P, Q	Elastic property anisotropy
P_c	Ultimate collapse pressure

Subscript

u,d	Undrained and drained case, respectively
GCS	Geographic coordinate system
PCS	In-situ principal stress coordinate system
BCS	Borehole coordinate system
BPCS	Bedding plane/material property coordinate system
eff	Biot's effective stresses
BP/bp	Bedding plane

Furthermore, immediately following wellbore excavation, pore fluids have not yet dissipated, rendering the instantaneous undrained response essential for understanding short-term wellbore stability, especially for low-permeability formations or the presence of filter-cake (Abousleiman and Cui, 1998; Bobet, 2011; Gao et al., 2016; Liu et al., 2022; Chen et al., 2023; Nordas et al., 2025). Consequently, a pressing need exists to develop a comprehensive anisotropic undrained wellbore stability model specifically tailored for arbitrarily inclined wells. However, a fully anisotropic undrained poroelastic response of an inclined borehole remains an open and unresolved issue in analytical solutions.

Previous research on analytical anisotropic wellbore stress solutions has predominantly employed the complex stress functions formulated by Lekhnitskii (1963) and Amadei (1983) to explore the influence of anisotropic mechanical properties (Hou et al., 2013). Extensions of these purely elastic frameworks have incorporated anisotropy in tensile and shear strengths to delineate safe mud weight window (Ma et al., 2019, 2022). Nonetheless, these models are fundamentally limited to dry rock conditions, thereby overlooking the crucial effects of pore pressure variations and poroelasticity on wellbore stability. Anisotropic undrained pore pressure response induced by depletion has been theoretically and experimentally investigated for shales (Duda et al., 2023; Soldal et al., 2025). While attempts to integrate poroelasticity into analytical anisotropic wellbore stability models have been partial; for instance, Liu et al. (2016) introduced an anisotropic wellbore stability model for inclined wells that incorporates poroelastic effects through anisotropic Biot's effective stress coefficients, but it does not consider the anisotropic undrained poroelastic response immediately post-drilling. Kanfar et al. (2015a, 2015b) first explored undrained pore pressure response in anisotropic formations, though their analysis was based on an isotropic solution. Subsequently, Raaen et al. (2019) utilized elastic Amadei stress solution to characterize the anisotropic undrained pore pressure response, further investigating the effect of undrained pore pressure on anisotropic wellbore stability (Asaka and Holt, 2021). However, accurate representation of the undrained poroelastic response necessitates the use of undrained poroelastic parameters rather than drained ones (Lu et al., 2025; Li et al., 2025). Li et al. (2025) focused exclusively on the undrained pore pressure response, the corresponding stress solution and subsequent short-term wellbore stability for such a fully anisotropic scenario remain insufficiently explored.

Although some analytical undrained solutions exist for specific cases in transversely isotropic formations, such as Bobet (2011) deriving closed-form solutions for undrained conditions in transversely isotropic lined circular tunnels, or Tran et al. (2022) and Lu et al. (2025) obtaining deterministic solutions for analogous conditions, these do not address the fully anisotropic inclined borehole problem. Furthermore, while recent numerical simulations by Qiu et al. (2023a, 2023b, 2024) and Peng et al. (2023) have examined the time-dependent pore pressure and stress states of inclined wells in anisotropic media, an analytical solution for the fully anisotropic wellbore stability issue remains elusive.

This study aims to derive an analytical anisotropic undrained poroelastic solution for an arbitrarily inclined borehole within transversely isotropic formations, encompassing all stress components and pore pressure variations. This study then evaluates the short-term collapse pressure by integrating anisotropic shear failure criteria with the derived anisotropic Biot's effective stresses. In the end, polar plots of short-term collapse pressure with varying wellbore trajectory and elastic property anisotropy are investigated.

2. Formulation

In this study, an arbitrary inclined borehole is drilled into a transversely isotropic poroelastic formation with an arbitrary dip azimuth and angle of bedding plane (BP), as shown in Fig. 1. When the borehole axis is neither perpendicular nor parallel to the isotropic plane in transversely isotropic formations, the wellbore problem becomes a fully anisotropic problem (Amadei, 1983). The initial vertical, minimum horizontal, and maximum horizontal stresses under PCS are denoted as σ_v, σ_h and σ_H, respectively. The initial pore pressure is denoted as p_0. Differing from previous purely elastic models (Kanfar et al., 2015a; Liu et al., 2016; Fang, 2018; Wang et al., 2022), the variation of pore pressure and corresponding undrained effects immediately after drilling are considered.

The in-situ stress and transversely isotropic poroelastic parameters need be converted into the borehole coordinate system (BCS). In Fig. 2, a geographic coordinate system (GCS) is used as a reference, where the positive directions of the X_e-, Y_e-, and Z_e- axes point north, east, and downward, respectively. The in-situ principal stress coordinate system (PCS) is defined by the azimuth of the maximum horizontal principal stress α_s and the angle between the vertical stress and the vertical direction β_s in Fig. 2(a), respectively. The borehole coordinate system (BCS) is determined by the wellbore azimuth and inclination angles (α_b, β_b) in Fig. 2(b), respectively. In the bedding plane (material property) coordinate system (BPCS), BP is defined by its dip direction and dip angle ($\alpha_{bp}+\pi$, β_{bp}) in Fig. 2(c), respectively.

Conversion of far-field in-situ stress (σ_h, σ_H, σ_v) into BCS as (σ_{xx}^b, σ_{yy}^b, σ_{zz}^b, τ_{yz}^b, τ_{xz}^b and τ_{xy}^b) can refer to Liu et al. (2016), which is described in Appendix A.

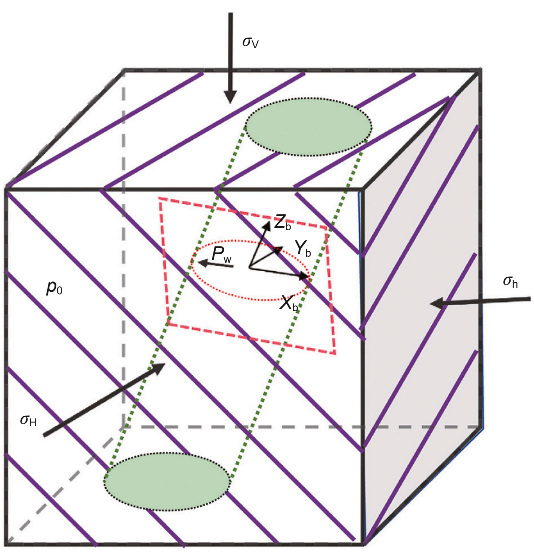

Fig. 1. A schematic diagram of an arbitrarily inclined borehole in transversely isotropic formations (Modified from Qiu et al. (2023a)).

2.1. Poroelastic constitutive law for transversely isotropic formations

The compressive stress is positive, and tensile stress is negative. Following the formality of a generalized Hooke's law, the linear poroelastic constitutive equations for transversely isotropic formations reads (Cheng, 2016)

$$\begin{aligned} &\boldsymbol{\sigma} = \boldsymbol{D}\varepsilon + \boldsymbol{\alpha} p, \\ &p = M(\zeta + \boldsymbol{\alpha\varepsilon}), \\ &\boldsymbol{\sigma} = \left[\sigma_x, \sigma_y, \sigma_z, \sigma_{yz}, \sigma_{xz}, \sigma_{xy}\right]^{\mathrm{T}}, \\ &\boldsymbol{\varepsilon} = \left[\varepsilon_x, \varepsilon_y, \varepsilon_z, \gamma_{yz}, \gamma_{xz}, \gamma_{xy}\right]^{\mathrm{T}}. \end{aligned} \tag{1}$$

where $\boldsymbol{D}$ and $\boldsymbol{\alpha}$ are the stiffness and Biot's effective stress coefficient matrices under BPCS, respectively. $\boldsymbol{\sigma}$, $\boldsymbol{\varepsilon}$ are the stress and strain tensors, ζ is fluid content variation per unit volume, M is Biot modulus, p is pore pressure, respectively. Under BPCS, drained stiffness matrix for the transversely isotropic formation can read as follows (Cheng, 2016; Qiu et al., 2023a)

$$\boldsymbol{D}_0 = \begin{bmatrix} D_{xx} & D_{xy} & D_{xz} & 0 & 0 & 0 \\ D_{xy} & D_{xx} & D_{xz} & 0 & 0 & 0 \\ D_{xz} & D_{xz} & D_{zz} & 0 & 0 & 0 \\ 0 & 0 & 0 & G' & 0 & 0 \\ 0 & 0 & 0 & 0 & G' & 0 \\ 0 & 0 & 0 & 0 & 0 & G \end{bmatrix} \tag{2}$$

with

$$\begin{aligned} &D_{xx} = \frac{E\left(E' - E\nu'^2\right)}{(1+\nu)\left(E' - E'\nu - 2E\nu'^2\right)}, \\ &D_{xy} = \frac{E\left(E'\nu + E\nu'^2\right)}{(1+\nu)\left(E' - E'\nu - 2E\nu'^2\right)}, \\ &D_{xz} = \frac{EE'\nu}{E' - E'\nu - 2E\nu'^2}, \\ &D_{zz} = \frac{E'^2(1-\nu)}{E' - E'\nu - 2E\nu'^2}, \\ &G = \frac{E}{2(1+\nu)}, G' = \frac{EE'}{E + E' + 2E'\nu'}. \end{aligned} \tag{3}$$

where, E, E' and ν, ν' are the drained elastic modulus and Poisson's ratio parallel and perpendicular to BP, respectively.

According to Cheng (2016), the solid grain bulk modulus K_s is a constant independent of the BP direction and K_f is the fluid bulk modulus, the Biot's effective stress coefficient matrix $\boldsymbol{\alpha}_0$ under BPCS and Biot modulus M are given as follows (Cheng, 2016; Qiu et al., 2023a):

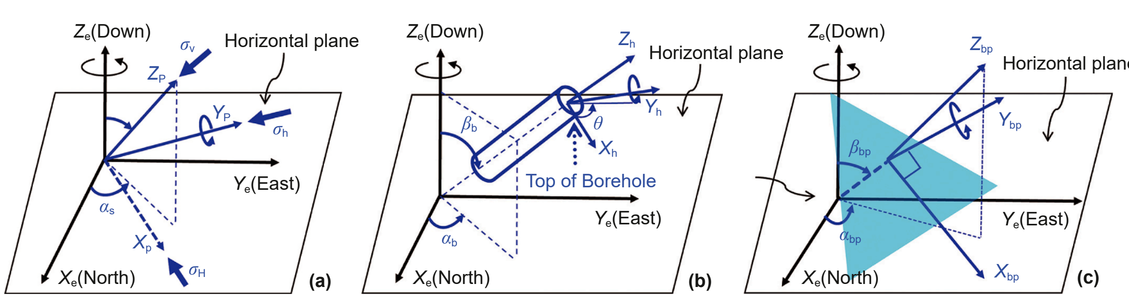

Fig. 2. Coordinate system schematics: (**a**) PCS; (**b**) BCS; (**c**) BPCS (Modified from Liu et al. (2016)).

$$[\boldsymbol{\alpha}_0]_{3\times3} = \begin{bmatrix} \alpha_\mathrm{h} & 0 & 0 \\ 0 & \alpha_\mathrm{h} & 0 \\ 0 & 0 & \alpha_\mathrm{v} \end{bmatrix} \tag{4}$$

$$M = K_\mathrm{s} \Big/ \left[\left(1 - \frac{K^*}{K_\mathrm{s}}\right) - \varphi\left(1 - \frac{K_\mathrm{s}}{K_\mathrm{f}}\right) \right] \tag{5}$$

with

$$\alpha_\mathrm{h} = 1 - (D_{xx} + D_{xy} + D_{xz}) / (3K_\mathrm{s}) \tag{6}$$

$$\alpha_\mathrm{v} = 1 - (2D_{xz} + D_{zz}) / (3K_\mathrm{s}) \tag{7}$$

$$K^* = \frac{(2D_{xx} + D_{zz} + 2D_{xy} + 4D_{xz})}{9} \tag{8}$$

where α_h, α_v are the Biot's effective stress coefficients parallel and perpendicular to the transverse plane, respectively. φ is porosity, K^* is bulk modulus.

2.2. Anisotropic undrained poroelastic constitutive law with an arbitrary wellbore trajectory

Under an undrained condition, the pore fluid has not yet escaped from the solid skeleton immediately after drilling, so $\zeta = 0$ is assumed in Eq. (1). Undrained constitutive law in Eq. (1) under BPCS can be rewritten as

$$\begin{aligned} p &= M[\boldsymbol{\alpha}_0]_{6\times1}\boldsymbol{\varepsilon}, \\ \boldsymbol{\sigma} &= \left(\boldsymbol{D}_0 + M[\boldsymbol{\alpha}_0]_{6\times1}[\boldsymbol{\alpha}_0]^\mathrm{T}_{6\times1}\right)\boldsymbol{\varepsilon}. \end{aligned} \tag{9}$$

with $[\boldsymbol{\alpha}_0]_{6\times1} = [\alpha_\mathrm{h}, \alpha_\mathrm{h}, \alpha_\mathrm{v}, 0, 0, 0]$.

Above stiffness constitutive law in Eq. (9) can be converted to compliance equation by matrix inversion as follows:

$$\begin{aligned} p &= M[\boldsymbol{\alpha}_0]_{1\times6}\boldsymbol{\varepsilon}, \\ \boldsymbol{\varepsilon} &= \left[\boldsymbol{A}_0^\mathrm{u}\right]_{6\times6}\boldsymbol{\sigma}. \end{aligned} \tag{10}$$

with $\boldsymbol{A}_0^\mathrm{u} = \left(\boldsymbol{D}_0 + M[\boldsymbol{\alpha}_0]_{6\times1}[\boldsymbol{\alpha}_0]^\mathrm{T}_{6\times1}\right)^{-1}$, which is in line with Cheng (2016). The superscript "u" denotes the undrained case in this study.

According to the bond coordinate transformation (Amadei, 1983; Gaede et al., 2012; Setiawan and Zimmerman, 2018; Fang, 2018; Vitali et al., 2020; Qiu et al., 2023a), the transformation process of the compliance tensor $\boldsymbol{A}_0^\mathrm{u}$ and Biot's effective stress coefficient matrix $\boldsymbol{\alpha}_\mathrm{t}$ under BCS can be expressed as follows:

$$\begin{aligned} \boldsymbol{A}_\mathrm{t}^\mathrm{u} &= [\boldsymbol{N}]_{6\times6}\boldsymbol{A}_0^\mathrm{u}\left[\boldsymbol{N}^\mathrm{T}\right]_{6\times6}, \\ \boldsymbol{\alpha}_\mathrm{t} &= [\boldsymbol{T}]_{3\times3}[\boldsymbol{\alpha}_0]_{3\times3}\left[\boldsymbol{T}^\mathrm{T}\right]_{3\times3}. \end{aligned} \tag{11}$$

where the transformation tensor $\boldsymbol{N}$ for the compliance tensor is given by Lekhnitskii (1963) as

$$\boldsymbol{N} = \begin{bmatrix} l_{11}^2 & l_{12}^2 & l_{13}^2 & l_{12}l_{13} & l_{13}l_{11} & l_{12}l_{11} \\ l_{21}^2 & l_{22}^2 & l_{23}^2 & l_{23}l_{22} & l_{23}l_{21} & l_{22}l_{21} \\ l_{31}^2 & l_{32}^2 & l_{33}^2 & l_{33}l_{32} & l_{33}l_{31} & l_{32}l_{31} \\ 2l_{31}l_{21} & 2l_{32}l_{22} & 2l_{33}l_{23} & l_{33}l_{22}+l_{32}l_{23} & l_{33}l_{21}+l_{31}l_{23} & l_{31}l_{22}+l_{32}l_{21} \\ 2l_{31}l_{11} & 2l_{32}l_{12} & 2l_{33}l_{13} & l_{33}l_{12}+l_{32}l_{13} & l_{33}l_{11}+l_{31}l_{13} & l_{31}l_{12}+l_{32}l_{11} \\ 2l_{21}l_{11} & 2l_{12}l_{22} & 2l_{13}l_{23} & l_{13}l_{22}+l_{12}l_{23} & l_{13}l_{21}+l_{11}l_{23} & l_{11}l_{22}+l_{12}l_{21} \end{bmatrix} \tag{12}$$

And the components l_{ij} (i, j = 1–3) are the direction cosines of vectors of the rectangular axes under BCS and BPCS, which are given as

$$\begin{aligned} &l_{11} = T(1,1),\ l_{12} = T(1,2),\ l_{13} = T(1,3) \\ &l_{21} = T(2,1),\ l_{22} = T(2,2),\ l_{23} = T(2,3) \\ &l_{31} = T(3,1),\ l_{32} = T(3,2),\ l_{33} = T(3,3) \end{aligned} \tag{13}$$

with

$$\begin{aligned} &\boldsymbol{T} = \boldsymbol{R}_2 \times \boldsymbol{R}_3^\mathrm{T}, \\ &\boldsymbol{R}_2 = \begin{bmatrix} \cos\alpha_\mathrm{b}\cos\beta_\mathrm{b} & \sin\alpha_\mathrm{b}\cos\beta_\mathrm{b} & -\sin\beta_\mathrm{b} \\ -\sin\alpha_\mathrm{b} & \cos\alpha_\mathrm{b} & 0 \\ \cos\alpha_\mathrm{b}\sin\beta_\mathrm{b} & \sin\alpha_\mathrm{b}\sin\beta_\mathrm{b} & \cos\beta_\mathrm{b} \end{bmatrix}, \\ &\boldsymbol{R}_3 = \begin{bmatrix} \cos\left(\alpha_\mathrm{bp} - \pi\right)\cos\beta_\mathrm{bp} & \sin\left(\alpha_\mathrm{bp} - \pi\right)\cos\beta_\mathrm{bp} & \sin\beta_\mathrm{bp} \\ -\sin\left(\alpha_\mathrm{bp} - \pi\right) & \cos\left(\alpha_\mathrm{bp} - \pi\right) & 0 \\ -\cos\left(\alpha_\mathrm{bp} - \pi\right)\sin\beta_\mathrm{bp} & -\sin\left(\alpha_\mathrm{bp} - \pi\right)\sin\beta_\mathrm{bp} & \cos\beta_\mathrm{bp} \end{bmatrix}. \end{aligned} \tag{14}$$

where transformation tensors $\boldsymbol{R}_2$, $\boldsymbol{R}_3$ from BPCS to BCS, are functions of wellbore trajectory (α_b, β_b) and dip direction and angle (α_bp+π, β_bp). The pore pressure p as a scalar quantity in Eq. (10) does not change after the transformation process. Eventually, the incremental anisotropic undrained poroelastic constitutive law for any wellbore trajectory under BCS is given as:

$$\begin{aligned} \Delta\boldsymbol{\varepsilon} &= \left[\boldsymbol{A}_\mathrm{t}^\mathrm{u}\right]_{6\times6}\Delta\boldsymbol{\sigma}^\mathrm{u}, \\ \Delta p &= M[\boldsymbol{\alpha}_\mathrm{t}]_{1\times6}\left[\boldsymbol{A}_\mathrm{t}^\mathrm{u}\right]_{6\times6}\Delta\boldsymbol{\sigma}^\mathrm{u} \end{aligned} \tag{15}$$

Cheng (1997, 2016) pointed out that there are twenty-one independent components in symmetric $\boldsymbol{A}_\mathrm{t}^\mathrm{u}$, six components in $\boldsymbol{\alpha}_\mathrm{t}$, and one M, with a total of 28 independent material constants for general anisotropy. When the borehole is not orthogonal to the isotropic plane, there also exist six non-zero Biot's effective stress coefficients under BCS rather than two independent values under BPCS after coordinate transformation in Eqs. (11–14), which reflects their projection into BCS.

2.2.1. Undrained poroelastic stress distribution on the borehole wall

Using Amadei's method (1983), the total undrained stress concentration on the borehole wall in the anisotropic medium can be derived as

$$\begin{aligned}
\sigma_x^{\mathrm{u}} &= \sigma_{xx}^{\mathrm{b}} + \Delta\sigma_x^{\mathrm{u}} = \sigma_{xx}^{\mathrm{b}} + 2Re\left[\mu_{1\mathrm{u}}^2\phi_{1\mathrm{u}}' + \mu_{2\mathrm{u}}^2\phi_{2\mathrm{u}}' + \lambda_3\mu_{3\mathrm{u}}^2\phi_{3\mathrm{u}}'\right], \\
\sigma_y^{\mathrm{u}} &= \sigma_{yy}^{\mathrm{b}} + \Delta\sigma_y^{\mathrm{u}} = \sigma_{yy}^{\mathrm{b}} + 2Re\left[\phi_{1\mathrm{u}}' + \phi_{2\mathrm{u}}' + \lambda_{3\mathrm{u}}\phi_{3\mathrm{u}}'\right], \\
\sigma_{yz}^{\mathrm{u}} &= \tau_{yz}^{\mathrm{b}} + \Delta\sigma_{yz}^{\mathrm{u}} = \tau_{yz}^{\mathrm{b}} - 2Re\left[\lambda_{1\mathrm{u}}\phi_{1\mathrm{u}}' + \lambda_{2\mathrm{u}}\phi_{2\mathrm{u}}' + \phi_{3\mathrm{u}}'\right], \\
\sigma_{xz}^{\mathrm{u}} &= \tau_{xz}^{\mathrm{b}} + \Delta\sigma_{xz}^{\mathrm{u}} = \tau_{xz}^{\mathrm{b}} + 2Re\left[\lambda_{1\mathrm{u}}\mu_{1\mathrm{u}}\phi_1' + \lambda_{2\mathrm{u}}\mu_{2\mathrm{u}}\phi_{2\mathrm{u}}' + \mu_{3\mathrm{u}}\phi_{3\mathrm{u}}'\right], \\
\sigma_{xy}^{\mathrm{u}} &= \tau_{xy}^{\mathrm{b}} + \Delta\sigma_{xy}^{\mathrm{u}} = \tau_{xy}^{\mathrm{b}} - 2Re\left[\mu_{1\mathrm{u}}\phi_{1\mathrm{u}}' + \mu_{2\mathrm{u}}\phi_{2\mathrm{u}}' + \lambda_{3\mathrm{u}}\mu_{3\mathrm{u}}\phi_{3\mathrm{u}}'\right], \\
\sigma_z^{\mathrm{u}} &= \sigma_{zz}^{\mathrm{b}} + \Delta\sigma_z^{\mathrm{u}} = \sigma_{zz}^{\mathrm{b}} - \frac{1}{A_{t33}^{\mathrm{u}}} \\
&\quad \left[A_{\mathrm{t}31}^{\mathrm{u}}\Delta\sigma_x^{\mathrm{u}} + A_{\mathrm{t}32}^{\mathrm{u}}\Delta\sigma_y^{\mathrm{u}} + A_{\mathrm{t}34}^{\mathrm{u}}\Delta\sigma_{yz}^{\mathrm{u}} + A_{\mathrm{t}35}^{\mathrm{u}}\Delta\sigma_{xz}^{\mathrm{u}} + A_{\mathrm{t}36}^{\mathrm{u}}\Delta\sigma_{xy}^{\mathrm{u}}\right],
\end{aligned} \tag{16}$$

where the in-situ stress components under BCS are denoted as σ_{xx}^{b}, $\sigma_{yy}^{\mathrm{b}}, \sigma_{zz}^{\mathrm{b}}, \tau_{yz}^{\mathrm{b}}, \tau_{xz}^{\mathrm{b}}$ and τ_{xy}^{b}, respectively. And the superscripts and subscripts "u" and "d" denote the undrained and drained cases in this study, respectively. Three undrained characteristic roots with pure or complex imaginary numbers $\mu_{i\mathrm{u}}$ (i = 1,2,3) is obtained using Lekhnitskii and Amadei's method. Interested readers can refer to Lekhnitskii (1963), Amadei (1983), Liu et al. (2016) and Wang et al. (2022) for further details. It should be noted that the undrained compliance matrix $\boldsymbol{A}_0^{\mathrm{u}}$ in Eq. (11) differs from the drained compliance one $\boldsymbol{D}^{-1}$ under BPCS. Consequently, the corresponding two matrices $\boldsymbol{A}_{\mathrm{t}}^{\mathrm{u}}$, $\boldsymbol{A}_{\mathrm{t}}^{\mathrm{d}}$ under BCS also differ, the three undrained characteristic roots $\mu_{i\mathrm{u}}$ (i = 1,2,3) are not identical to the drained ones $\mu_{i\mathrm{d}}$ (i = 1,2,3). This distinction will be discussed further in Section 3.2.

And the analytical functions ($\phi_{i\mathrm{u}}'(i = 1,2,3)$) is determined by the boundary conditions, which are given as (Liu et al., 2016)

$$\begin{aligned}
\phi_{1\mathrm{u}}' &= \frac{1}{2\Delta_{\mathrm{u}}(\mu_{1\mathrm{u}}\cos\theta - \sin\theta)}\left[D'(\lambda_{2\mathrm{u}}\lambda_{3\mathrm{u}} - 1)\right. \\
&\quad \left. + E'(\mu_{2\mathrm{u}} - \lambda_{2\mathrm{u}}\lambda_{3\mathrm{u}}\mu_{3\mathrm{u}}) + F'(\mu_{3\mathrm{u}} - \mu_{2\mathrm{u}})\lambda_{3\mathrm{u}}\right], \\
\phi_{2\mathrm{u}}' &= \frac{1}{2\Delta_{\mathrm{u}}(\mu_{2\mathrm{u}}\cos\theta - \sin\theta)}\left[D'(1 - \lambda_{1\mathrm{u}}\lambda_{3\mathrm{u}})\right. \\
&\quad \left. + E'(\lambda_{1\mathrm{u}}\lambda_{3\mathrm{u}}\mu_{3\mathrm{u}} - \mu_{1\mathrm{u}}) + F'(\mu_{1\mathrm{u}} - \mu_{3\mathrm{u}})\lambda_{3\mathrm{u}}\right], \\
\phi_{3\mathrm{u}}' &= \frac{1}{2\Delta_{\mathrm{u}}(\mu_{3\mathrm{u}}\cos\theta - \sin\theta)}\left[D'(\lambda_{1\mathrm{u}} - \lambda_{2\mathrm{u}})\right. \\
&\quad \left. + E'(\lambda_{2\mathrm{u}}\mu_{1\mathrm{u}} - \lambda_{1\mathrm{u}}\mu_{2\mathrm{u}}) + F'(\mu_{2\mathrm{u}} - \mu_{1\mathrm{u}})\right],
\end{aligned} \tag{17}$$

with

$$\begin{aligned}
D' &= \left(P_{\mathrm{w}} - \sigma_{xx}^{\mathrm{b}}\right)\cos\theta - \tau_{xy}^{\mathrm{b}}\sin\theta - \mathrm{i}\left[\left(P_{\mathrm{w}} - \sigma_{xx}^{\mathrm{b}}\right)\sin\theta + \tau_{xy}^{\mathrm{b}}\cos\theta\right], \\
E' &= -\left(P_{\mathrm{w}} - \sigma_{yy}^{\mathrm{b}}\right)\sin\theta + \tau_{xy}^{\mathrm{b}}\cos\theta - \mathrm{i}\left[\left(P_{\mathrm{w}} - \sigma_{yy}^{\mathrm{b}}\right)\cos\theta + \tau_{xy}^{\mathrm{b}}\sin\theta\right], \\
F' &= -\tau_{xz}^{\mathrm{b}}\cos\theta - \tau_{yz}^{\mathrm{b}}\sin\theta - \mathrm{i}\left[\tau_{yz}^{\mathrm{b}}\cos\theta - \tau_{xz}^{\mathrm{b}}\sin\theta\right], \\
\Delta_{\mathrm{u}} &= \mu_{2\mathrm{u}} - \mu_{1\mathrm{u}} + \lambda_{2\mathrm{u}}\lambda_{3\mathrm{u}}(\mu_{1\mathrm{u}} - \mu_{3\mathrm{u}}) + \lambda_{1\mathrm{u}}\lambda_{3\mathrm{u}}(\mu_{3\mathrm{u}} - \mu_{2\mathrm{u}}).
\end{aligned} \tag{18}$$

The complex variables $\lambda_{i\mathrm{u}}(i=1,2,3)$ are defined as

$$\begin{aligned}
&\lambda_{1\mathrm{u}} = -\frac{l_{3\mathrm{u}}(\mu_{i\mathrm{u}})}{l_{2\mathrm{u}}(\mu_{i\mathrm{u}})}, \lambda_2 = -\frac{l_{3\mathrm{u}}(\mu_{i\mathrm{u}})}{l_{2\mathrm{u}}(\mu_{i\mathrm{u}})}, \lambda_3 = -\frac{l_{3\mathrm{u}}(\mu_{i\mathrm{u}})}{l_{4\mathrm{u}}(\mu_{i\mathrm{u}})}. \\
&l_{2\mathrm{u}}(\mu_{i\mathrm{u}}) = \beta_{44}^{\mathrm{u}} - 2\beta_{45}^{\mathrm{u}}\mu_{i\mathrm{u}} + \beta_{55}^{\mathrm{u}}\mu_{i\mathrm{u}}{}^2, \\
&l_{3\mathrm{u}}(\mu_{i\mathrm{u}}) = -\beta_{24}^{\mathrm{u}} + (\beta_{25}^{\mathrm{u}} + \beta_{46}^{\mathrm{u}})\mu_{i\mathrm{u}} - (\beta_{14}^{\mathrm{u}} + \beta_{56}^{\mathrm{u}})\mu_{i\mathrm{u}}{}^2 + \beta_{15}^{\mathrm{u}}\mu_{i\mathrm{u}}{}^3, \\
&l_{4\mathrm{u}}(\mu_{i\mathrm{u}}) = -\beta_{22}^{\mathrm{u}} - 2\beta_{26}^{\mathrm{u}}\mu_{i\mathrm{u}} + (2\beta_{12}^{\mathrm{u}} + \beta_{66}^{\mathrm{u}})\mu_{i\mathrm{u}}{}^2 - 2\beta_{16}^{\mathrm{u}}\mu_{i\mathrm{u}}{}^3 + \beta_{11}^{\mathrm{u}}\mu_{i\mathrm{u}}{}^4,
\end{aligned} \tag{19}$$

where β_{ij} is the reduced strain coefficients from compliance matrix $\boldsymbol{A}_{\mathrm{t}}^{\mathrm{u}}$ defined as:

$$\beta_{ij}^{\mathrm{u}} = A_{\mathrm{t}ij}^{\mathrm{u}} - \frac{A_{\mathrm{t}i3}^{\mathrm{u}}A_{\mathrm{t}j3}^{\mathrm{u}}}{A_{\mathrm{t}33}^{\mathrm{u}}}, \quad (i,j = 1,2,...,6) \tag{20}$$

Table 1
Input parameters from Liu et al. (2016) and Gao et al. (2021).

Parameter	Unit	Value	Parameter	Unit	Value
Maximum horizontal principal stress σ_{H}	MPa	45.55	Offset angle of σ_{H}, α_{s}	°	135
Minimum horizontal principal stress σ_{h}	MPa	34.86	Offset angle of σ_{v}, β_{s}	°	0
Overburden stress σ_{v}	MPa	37.17	Formation pressure p_0	MPa	17.76
Elastic modulus normal to BP E'	GPa	P*30	Wellbore pressure P_{w}	MPa	25
Elastic modulus in BP E	GPa	30	Grain solid modulus K_{s}	GPa	83
Poisson's ratio normal to BP ν'	-	Q*0.2	Fluid modulus K_{f}	GPa	3.29
Poisson's ratio in BP ν	-	0.2	Dip angle of BP β_{bp}	°	45
Cohesion of intact rock c	MPa	8.2	Dip direction of BP $\alpha_{\mathrm{bp}}+\pi$	°	315
Cohesion of BP c_{w}	MPa	2.07	Friction angle of intact rock ϕ	°	31
Wellbore inclination β_{b}	°	30	Friction angle of BP ϕ_{w}	°	26.6
Wellbore azimuth α_{b}	°	45	Porosity φ	-	0.05

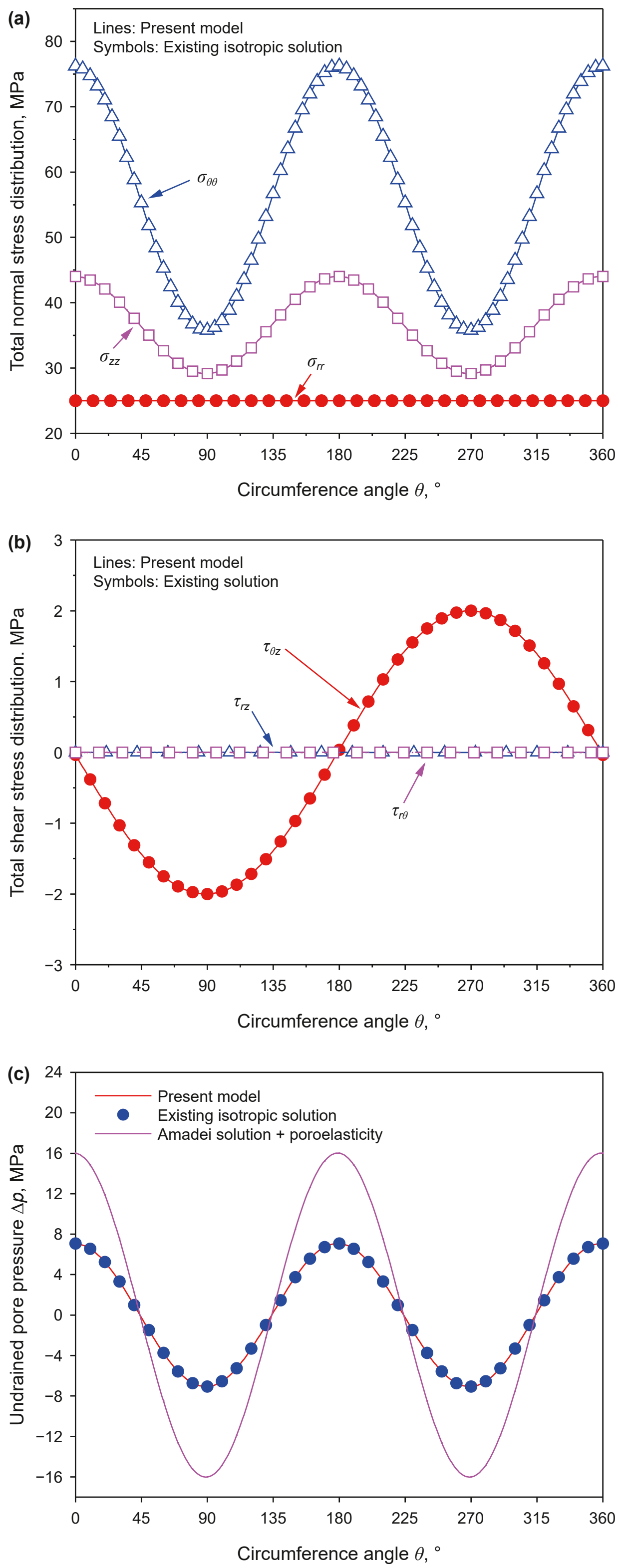

Fig. 3. Comparison of undrained stress and pore pressure distributions between present and existing solutions for the isotropic case.

2.2.2. *Undrained poroelastic response utilizing drained Amadei stress solution*

While the existing model neglected the difference between the undrained and elastic/drained stress solution (Amadei, 1983; Liu et al., 2016). The existing elastic solution is given by Amadei solution (1983) with drained parameters:

$$
\begin{aligned}
&\sigma_x^{\rm d}=\sigma_{xx}^{\rm b}+\Delta\sigma_x^{\rm d}=\sigma_{xx}^{\rm b}+2Re\left[\mu_{1\rm d}^2\phi_{1\rm d}^{'}+\mu_{2\rm d}^2\phi_{2\rm d}^{'}+\lambda_{3\rm d}\mu_{3\rm d}^2\phi_{3\rm d}^{'}\right],\\
&\sigma_y^{\rm d}=\sigma_{yy}^{\rm b}+\Delta\sigma_y^{\rm d}=\sigma_{yy}^{\rm b}+2Re\left[\phi_{1\rm d}^{'}+\phi_{2\rm d}^{'}+\lambda_{3\rm d}\phi_{3\rm d}^{'}\right],\\
&\sigma_{yz}^{\rm d}=\tau_{yz}^{\rm b}+\Delta\sigma_{yz}^{\rm d}=\tau_{yz}^{\rm b}-2Re\left[\lambda_{1\rm d}\phi_{1\rm d}^{'}+\lambda_{2\rm d}\phi_{2\rm d}^{'}+\phi_{3\rm d}^{'}\right],\\
&\sigma_{xz}^{\rm d}=\tau_{xz}^{\rm b}+\Delta\sigma_{xz}^{\rm d}=\tau_{xz}^{\rm b}+2Re\left[\lambda_{1\rm d}\mu_{1\rm d}\phi_{1\rm d}^{'}+\lambda_{2\rm d}\mu_{2\rm d}\phi_{2\rm d}^{'}+\mu_{3\rm d}\phi_{3\rm d}^{'}\right],\\
&\sigma_{xy}^{\rm d}=\tau_{xy}^{\rm b}+\Delta\sigma_{xy}^{\rm d}=\tau_{xy}^{\rm b}-2Re\left[\mu_{1\rm d}\phi_{1\rm d}^{'}+\mu_{2\rm d}\phi_{2\rm d}^{'}+\lambda_{3\rm d}\mu_{3\rm d}\phi_{3\rm d}^{'}\right],\\
&\sigma_z^{\rm d}=\sigma_{zz}^{\rm b}+\Delta\sigma_z^{\rm d}=\sigma_{zz}^{\rm b}-\frac{1}{A_{t33}^{\rm d}}\left[A_{\rm t31}^{\rm d}\Delta\sigma_x^{\rm d}+A_{\rm t32}^{\rm d}\Delta\sigma_y^{\rm d}+A_{\rm t34}^{\rm d}\Delta\sigma_{yz}^{\rm d}\right.\\
&\left.+A_{\rm t35}^{\rm d}\Delta\sigma_{xz}^{\rm d}+A_{\rm t36}^{\rm d}\Delta\sigma_{xy}^{\rm d}\right],
\end{aligned}
\tag{21}
$$

where the common elastic drained parameters are used with the superscript and subscript “d”. Corresponding drained parameters in Eqs. (16–20) is given by Amadei (1983) and Liu et al. (2016). Raaen et al. (2019) used anisotropic Skempton coefficients and elastic Amadei stress solution to obtain the undrained pore pressure distribution. In similar, the induced undrained pore pressure distribution using elastic Amadei stress solution and six non-zero Biot's effective stress coefficients is given as:

$$
\Delta p^{\rm d}=M[\boldsymbol{\alpha}_{\rm t}]_{1\times 6}\left[\boldsymbol{A}_{\rm t}^{\rm d}\right]_{6\times 6}\left[\Delta\boldsymbol{\sigma}^{\rm d}\right]_{6\times 1}
\tag{22}
$$

2.2.3. *Stress distribution on the borehole wall under BCS*

Stress components on the borehole wall in cylindrical coordinate system can be given as (Hou et al., 2013; Zhang et al., 2021; Ma et al., 2022)

$$
\begin{cases}
\sigma_{rr}=\sigma_{xx}\cos^2\theta+\sigma_{yy}\sin^2\theta+\tau_{xy}\sin 2\theta\\
\sigma_{\theta\theta}=\sigma_{xx}\sin^2\theta+\sigma_{yy}\cos^2\theta-\tau_{xy}\sin 2\theta\\
\sigma_{zz}=\sigma_{zz}\\
\tau_{r\theta}=-0.5\sigma_{xx}\sin 2\theta+0.5\sigma_{y}\sin 2\theta+\tau_{xy}\cos 2\theta\\
\tau_{rz}=\tau_{yz}\cos\theta-\tau_{xz}\sin\theta\\
\tau_{\theta z}=\tau_{yz}\sin\theta+\tau_{xz}\cos\theta
\end{cases}
\tag{23}
$$

where, σ_{rr}, $\sigma_{\theta\theta}$ and σ_{zz} are radial, hoop and axial stress components, and $\tau_{r\theta}$, τ_{rz}, $\tau_{\theta z}$ are three shear stress components, respectively. θ is angle of circumference. According to Eq. (23), the shear stress components $\tau_{r\theta}=\tau_{rz}=0$, thus the radial stress on the borehole wall $\sigma_{rr}=P_{\rm w}$ is a principal stress. Consequently, the three principal stresses can be expressed as:

$$
\begin{cases}
S_1=\dfrac{1}{2}(\sigma_{\theta\theta}+\sigma_{zz})+\dfrac{1}{2}\sqrt{(\sigma_{\theta\theta}-\sigma_{zz})^2+4\tau_{\theta z}^2}\\
S_2=\dfrac{1}{2}(\sigma_{\theta\theta}+\sigma_{zz})-\dfrac{1}{2}\sqrt{(\sigma_{\theta\theta}-\sigma_{zz})^2+4\tau_{\theta z}^2}\\
S_3=P_{\rm w}
\end{cases}
\tag{24}
$$

The undrained pore pressure without any pore pressure dissipation is assumed to occur when the wellbore is instantaneously excavated. Considering the impermeable wellbore boundary conditions, the corresponding ultimate pore pressure variation at/near the borehole wall are given as

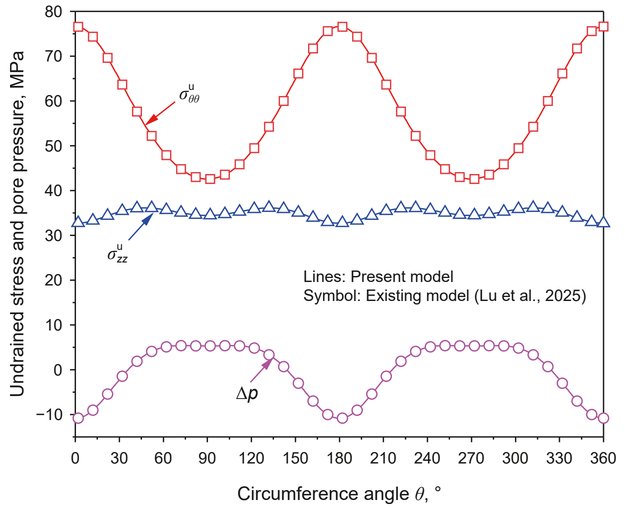

Fig. 4. Comparison of undrained stress and pore pressure distributions between present and existing solutions for the transversely isotropic case.

$$p = p_0 + \Delta p \tag{25}$$

Considering the anisotropic poroelastic effect, Biot's effective stress tensor on the borehole wall is given as

$$\boldsymbol{\sigma}_{\mathrm{b}}^{\mathrm{eff}} = \begin{Bmatrix} \sigma_{xx} & \tau_{xy} & \tau_{xz} \\ \tau_{xy} & \sigma_{y} & \tau_{yz} \\ \tau_{xz} & \tau_{yz} & \sigma_{z} \end{Bmatrix} - \begin{Bmatrix} \alpha_{xx} & \alpha_{xy} & \alpha_{xz} \\ \alpha_{xy} & \alpha_{yy} & \alpha_{yz} \\ \alpha_{xz} & \alpha_{yz} & \alpha_{zz} \end{Bmatrix} p \tag{26}$$

where α_{ij} $(i, j = x, y, z)$ is the element in anisotropic Biot's effective stress coefficient matrix $\boldsymbol{\alpha}_{\mathrm{t}}$ in Eq. (11). Differing from the isotropic case, Biot's effective stress coefficients α_{xy}, α_{yz}, α_{xz} related to shear stress components under BCS may not necessarily be zero, implying that all induced stress components in $\Delta\boldsymbol{\sigma}^{\mathrm{u}}$ both influence undrained pore pressure variations in Eq. (15). The normal stress variations may be induced by shear stress components in the anisotropic case, which is often called as shear-tension coupling effect (Liu et al., 2016). Consequently, the anisotropic poroelastic response should consider the comprehensive impacts of shear-tension and fluid-solid coupling effects.

In addition, due to the six non-zero anisotropic Biot's effective stress coefficients, it can be expected that Biot's effective radial stress component may not be a principal stress. Then following the method by Zhang et al. (2015), the three effective principal stresses on the borehole wall are equivalent to the three eigenvalues of the effective stress tensor $\boldsymbol{\sigma}_{\mathrm{b}}^{\mathrm{eff}}$ in Eq. (26), which can be obtained by:

$$\det\left(\boldsymbol{\sigma}_{\mathrm{b}}^{\mathrm{eff}} - S^{\mathrm{eff}}\mathbf{E}\right) = 0 \tag{27}$$

where $\mathbf{E}$ is a unit matrix, and $S_i^{\mathrm{eff}} (i = 1 - 3)$ are the corresponding three eigenvalues.

2.3. Determination of collapse pressure

2.3.1. Shear failure of intact matrix

Considering the effect of the intermediate principal stress, rock failure potential based on 3D Mogi-Coulomb criterion developed by Al-Ajmi and Zimmerman (2005) can be given as

$$F_{\mathrm{m}} = \frac{1}{3}\sqrt{\left(S_2^{\mathrm{eff}} - S_3^{\mathrm{eff}}\right)^2 + \left(S_2^{\mathrm{eff}} - S_1^{\mathrm{eff}}\right)^2 + \left(S_1^{\mathrm{eff}} - S_3^{\mathrm{eff}}\right)^2} - a - b\frac{S_1^{\mathrm{eff}} + S_3^{\mathrm{eff}}}{2},$$
$$a = \frac{2\sqrt{2}c\cos\phi}{3},\ b = \frac{2\sqrt{2}c\sin\phi}{3} \tag{28}$$

where c and ϕ are the rock cohesion and friction angle of matrix, $S_i^{\mathrm{eff}} (i = 1 - 3)$ are the maximum, median, and minimum eigenvalues in Eq. (27), respectively.

2.3.2. Shear failure of weak BP

Based on the Mohr-Coulomb criterion, failure potential for the weak BP by Lee et al. (2012) is given as:

$$F_{\mathrm{bp}} = \sqrt{\left(\tau_{zx}^{\mathrm{bp}}\right)^2 + \left(\tau_{zy}^{\mathrm{bp}}\right)^2} - c_{\mathrm{w}} - \tan(\phi_{\mathrm{w}})\sigma_{zz}^{\mathrm{bp}} \tag{29}$$

where c_{w} and ϕ_{w} are the cohesion and friction coefficient of BP, respectively. $\tau_{\mathrm{W}}^{\mathrm{bp}}$ and $\sigma_{\mathrm{W}}^{\mathrm{bp}}$ are the effective shear and normal stresses on BP, respectively. Noted that the Biot's effective stress coefficients related to shear stress components may be non-zero values in Eq. (26). Thus, the shear stresses in Eq. (29) are Biot's effective stresses. To determine the failure potential of weak BP, the effective stress tensor under BPCS should be obtained by transformation from BCS, which is given as (Liu et al., 2016)

Table 2
Additional input parameters in Section 3.1.2.

Parameter	Unit	Value	Parameter	Unit	Value
Wellbore azimuth α_{b}	°	45	Inclination angle β_{b}	°	90
Dip direction α_{bp}	°	0	Dip angle β_{bp}	°	0
Elastic anisotropy P	-	0.4	Poisson's ratio anisotropy Q	-	1.5

Table 3
Anisotropic Biot's effective stress coefficients under BCS with varying wellbore trajectories.

Boit's effective stress coefficients	α_{xx}	α_{yy}	α_{zz}	α_{yz}	α_{xz}	α_{xy}
$\alpha_{\mathrm{b}} = 45°$, $\beta_{\mathrm{b}} = 30°$	0.569	0.618	0.602	−0.057	−0.028	−0.033
$\alpha_{\mathrm{b}} = 90°$, $\beta_{\mathrm{b}} = 30°$	0.633	0.585	0.570	−0.024	−0.037	0.051
$\alpha_{\mathrm{b}} = \alpha_{\mathrm{bp}} \pm \pi$, $\beta_{\mathrm{b}} + \beta_{\mathrm{bp}} = 90°$	0.683	0.552	0.552	0	0	0
$\alpha_{\mathrm{b}} = \alpha_{\mathrm{bp}}$, $\beta_{\mathrm{b}} = \beta_{\mathrm{bp}}$	0.552	0.552	0.683	0	0	0

$$\boldsymbol{\sigma}_{\mathrm{bp}}^{\mathrm{eff}} = \boldsymbol{R}_3 \times \boldsymbol{R}_2^{\mathrm{T}} \times \boldsymbol{\sigma}_{\mathrm{b}}^{\mathrm{eff}} \times \boldsymbol{R}_2 \times \boldsymbol{R}_3^{\mathrm{T}} = \begin{Bmatrix} \sigma_{xx}^{\mathrm{bp}} & \tau_{xy}^{\mathrm{bp}} & \tau_{xz}^{\mathrm{bp}} \\ \tau_{yx}^{\mathrm{bp}} & \sigma_{yy}^{\mathrm{bp}} & \tau_{yz}^{\mathrm{bp}} \\ \tau_{zx}^{\mathrm{bp}} & \tau_{zy}^{\mathrm{bp}} & \sigma_{zz}^{\mathrm{bp}} \end{Bmatrix} \tag{30}$$

where $\boldsymbol{\sigma}_{\mathrm{bp}}^{\mathrm{eff}}$ is the Biot's effective stress tensor under BPCS.

3. Anisotropic undrained poroelastic solution of an arbitrary inclined borehole

3.1. Model validation

Two anisotropy indexes $P = E'/E$ and $Q = \nu'/\nu$ are used to characterize the degree of elastic anisotropy. The analytical drained solution has been validated by finite element method by Gaede et al. (2012). To further validate the accuracy of the present undrained model, models comparisons with isotropic and transversely isotropic solutions, as well as anisotropic Biot's effective stress coefficients, are made. The input parameters utilized in this study are listed in Table 1.

3.1.1. Model comparison in isotropic case

The validity of the present model in capturing the undrained poroelastic response is first confirmed through comparison with the isotropic scenario ($P = Q = 1$), demonstrating strong concordance in Fig. 3. Detailed undrained and drained poroelastic solutions for an inclined borehole within isotropic formations are presented in Appendix B. Crucially, the pore pressure distribution predicted using the drained/elastic stress solution (magenta line in Fig. 3(c)) in Eq. (22) substantially overestimates the undrained pore pressure response. While under dry or drained condition, the undrained pore pressure response is zero, underscoring the critical role of the undrained poroelastic effect immediately after drilling, which pure elastic Amadei solution fails to capture.

3.1.2. Model comparison for a horizontal borehole in transversely isotropic formations

To validate the proposed model in an anisotropic context, its predictions for a horizontal borehole in a transversely isotropic formation are made. The undrained stress solution of a horizontal borehole drilled along BP is presented in Appendix C. Fig. 4 presents the model comparison between the present and existing undrained solution (Lu et al., 2025), which shows strong agreement. For this comparison, some input parameters from Table 1 are used, with additional parameters listed in Table 2. Note that the existing solution by Lu et al. (2025) is limited to a specific case where the borehole axis is drilled along BP and aligned with a principal horizontal stress direction. In contrast, the present model offers a more general framework, accommodating arbitrary wellbore trajectories relative to the material and stress anisotropy. Profile of the anisotropic undrained pore pressure does not necessarily exhibit significant azimuthal dependence and symmetric distribution as the isotropic case in Fig. 4(c), where peak values occur at 0°/90°. The in-plane characteristic roots in the present model are reciprocals of those in the existing solution in Eq. (C-3), due to the different coordinate system. While the three characteristic roots, including in-plane and out-of-plane problems, do not need to be specified in the present model, since the corresponding coefficients related to all characteristic roots both exist in Eqs. (16) and (17).

This validation case, demonstrating agreement with a specific anisotropic solution, highlights that when the borehole axis deviates from orthogonality to BP, the fully anisotropic undrained poroelastic response becomes intricately dependent on the wellbore trajectory, influenced by the coordinate transformation described in Eqs. (11–14). Such complexities, arising from the interplay between borehole orientation and material anisotropy,

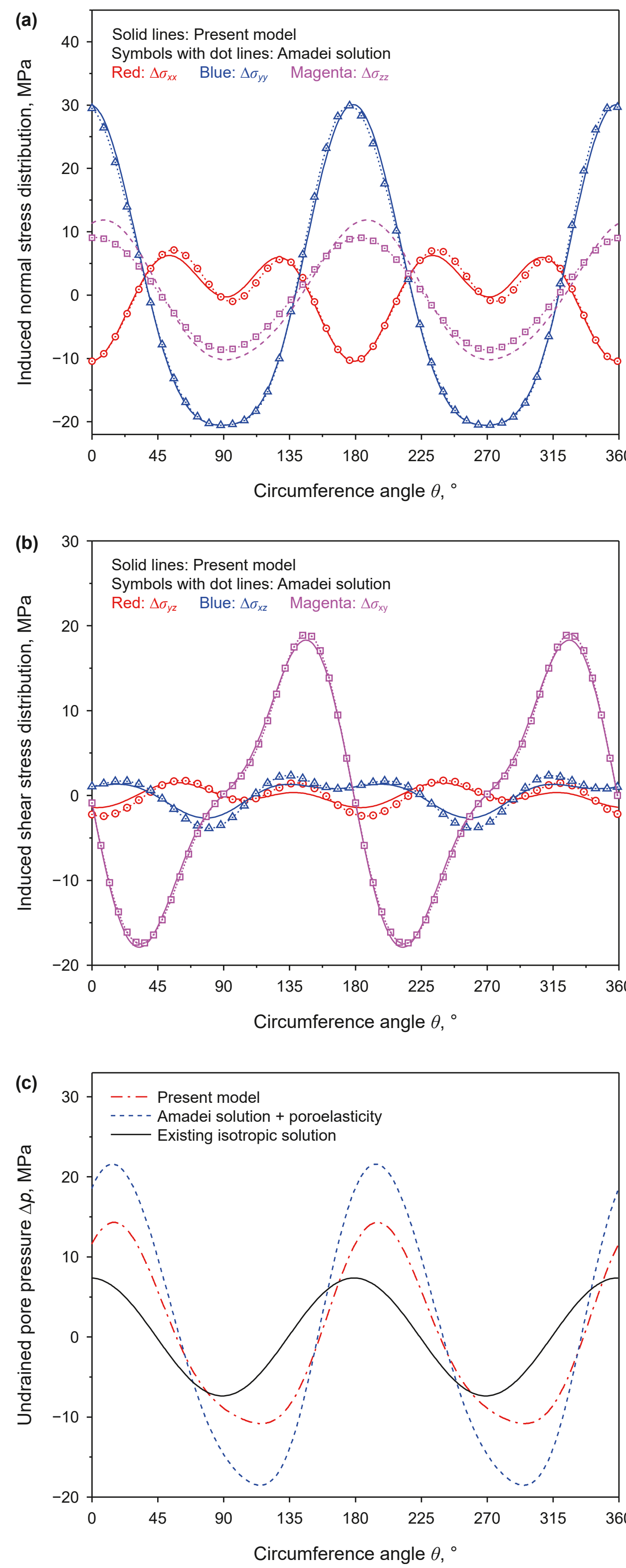

Fig. 5. Comparison of undrained stress and pore pressure distribution on the borehole wall with $P = 0.4$, $Q = 1.5$.

Table 4
Characteristic roots under undrained/drained conditions with $P = 0.4$, $Q = 1.5$

Cases	Undrained case	Drained case
Characteristic root μ_1	0.0081 + 1.2179i	0.1308 + 1.0858i
Characteristic root μ_2	0.1308 + 1.0858i	0.1300 + 1.0854i
Characteristic root μ_3	0.1800 + 0.9357i	−0.0453 + 0.9643i

underscore the critical need for the comprehensive, fully anisotropic wellbore stability model proposed herein.

3.1.3. Validation of anisotropic Biot's effective stress coefficients

In certain scenarios, the six non-zero anisotropic Biot's effective stress coefficients under BCS reduce to the two independent values under BPCS, as illustrated in Table 3. This simplification can occur, when the axis of the material's rotational symmetry is either in parallel with or perpendicular to the borehole axis (Liu and Abousleiman, 2020). There are two distinct conditions.

(1) When the borehole is drilled parallel to BP, and the borehole azimuth aligns with the dip direction of BP, where the sum of the wellbore inclination angle and the bedding dip angle is 90° ($\alpha_b = \alpha_{bp} \pm \pi$, $\beta_b + \beta_{bp} = 90°$).

(2) When the borehole is drilled perpendicular to BP ($\alpha_b = \alpha_{bp}$, $\beta_b = \beta_{bp}$). Under this condition, the in-plane Biot's effective stress coefficients (α_{xx}, α_{yy}) under BCS are equal to α_h, and the axial one (α_{zz}) equals α_v in Eqs. (4–8), while all other components vanish. This borehole problem can be solved using the proposed solution by Cui et al. (1998), where the three characteristic roots all degrade into 1i.

Conversely, in all other general cases not covered by these specific conditions, all six non-zero anisotropic Biot's effective stress coefficients must be considered. The calculated Biot's effective stress coefficients in Table 3 further validates the accuracy of the present model.

3.2. Difference of undrained and drained poroelastic response

Fig. 5 shows the induced stress and pore pressure distributions on the borehole wall with $P = 0.4$, $Q = 1.5$, as formulated in Eqs. (15) and (16). As depicted in Fig. 5(a) and (b), the induced normal and shear stress distributions predicted by the present model slightly diverge from those predicted by classical drained Amadei solution. This discrepancy arises from variations in three characteristic roots under the two conditions, as presented in Table 4, which result in differing induced stress distributions in

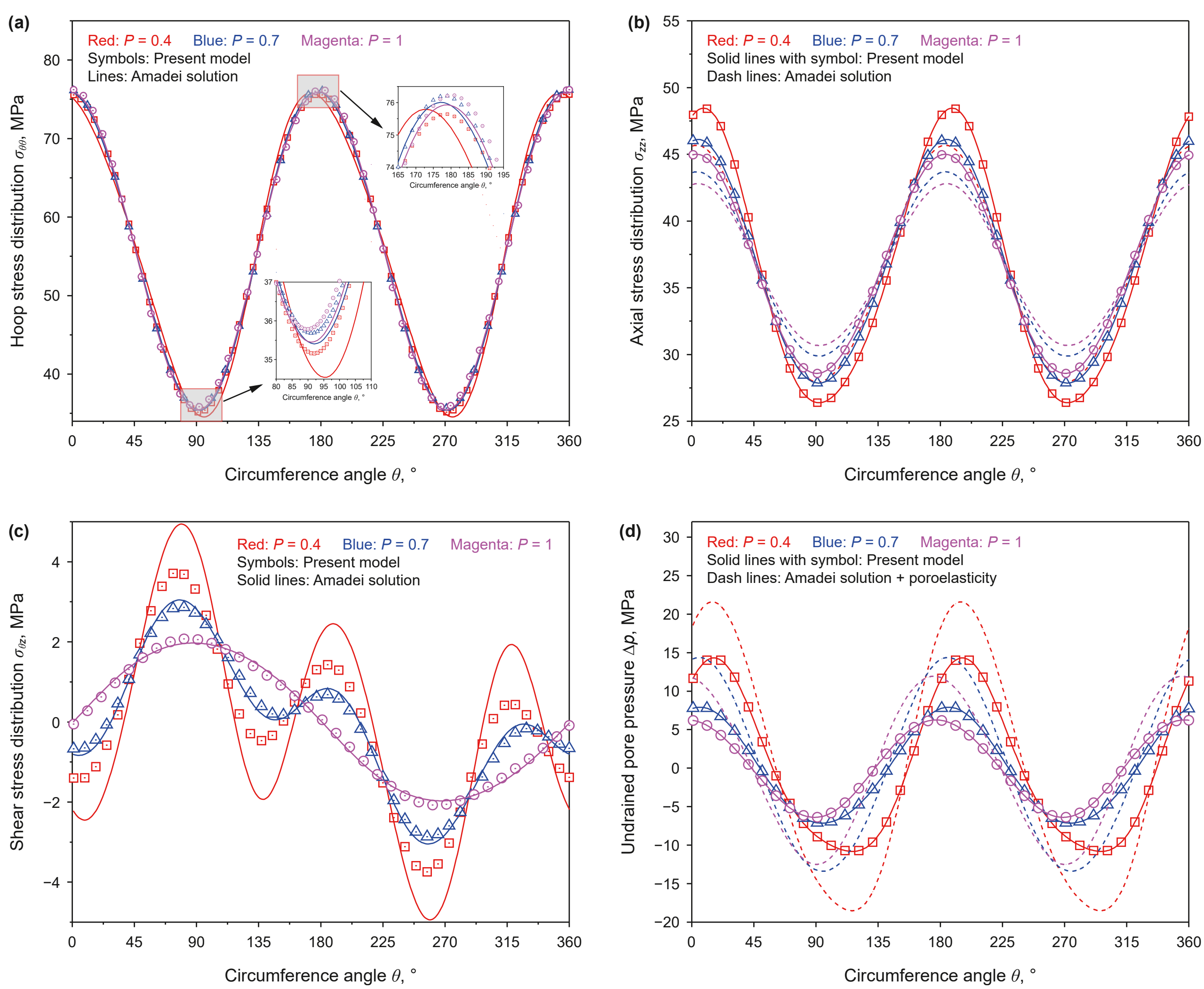

Fig. 6. Influence of elastic modulus anisotropy on the poroelastic response ($Q = 1.5$, $P_w = 25$ MPa).

Eqs. (16) and (21). Consequently, drained Amadei solution (Amadei, 1983; Setiawan and Zimmerman, 2018; Fang, 2018), fails to accurately represent the undrained stress distribution. In addition to the differing induced stress components, discrepancies between the drained and undrained compliance matrix in Eq. (12) further exacerbate deviations in the (induced) undrained pore pressure distribution in Fig. 5(c). When accounting for elastic anisotropy, the classical isotropic undrained pore pressure solution presented in Eq. (B-4) introduces significant errors in predicting the anisotropic undrained pore pressure response. In contrast, the "Amadei solution + poroelasticity" approach will significantly overestimate the undrained pore pressure response, as demonstrated by doted blue line in Fig. 5(c). These significant discrepancies between the undrained and drained solutions underscore the critical importance of considering undrained poroelastic constitutive framework for accurate anisotropic undrained pore pressure response analysis.

3.3. Parametric analysis of anisotropic undrained poroelastic response

This section presents a comprehensive parametric analysis of the undrained poroelastic response, focusing on the unique insights provided by the fully anisotropic undrained stress solution. This approach is critical as drained Amadei solution, inherently overlook the complex solid-fluid couplings, which are vital for an accurate representation of the anisotropic Skempton effect.

3.3.1. Influence of elastic property anisotropy

(1) **Elastic modulus anisotropy**

Fig. 6 presents the profiles of wellbore stresses and pore pressure on the borehole wall (excluding the constant radial stress component) under varying elastic modulus anisotropy (P). With increasing elastic modulus anisotropy ($P \to 0$), the differences in hoop stress distributions under these two conditions can be neglected in Fig. 6(a), while those of axial and shear stress distributions in Fig. 6(b) and (c) should be paid more attention to. Furthermore, the distribution ranges of axial and shear stress components increase with increasing elastic modulus anisotropy, suggesting that elastic modulus anisotropy intensifies the heterogeneity of stress patterns in both the present and Amadei solutions. Compared to Amadei solution, the undrained condition enhances the heterogeneity of stress distributions (Fig. 6(b) and (c)), thereby underscoring the importance of the undrained poroelastic response.

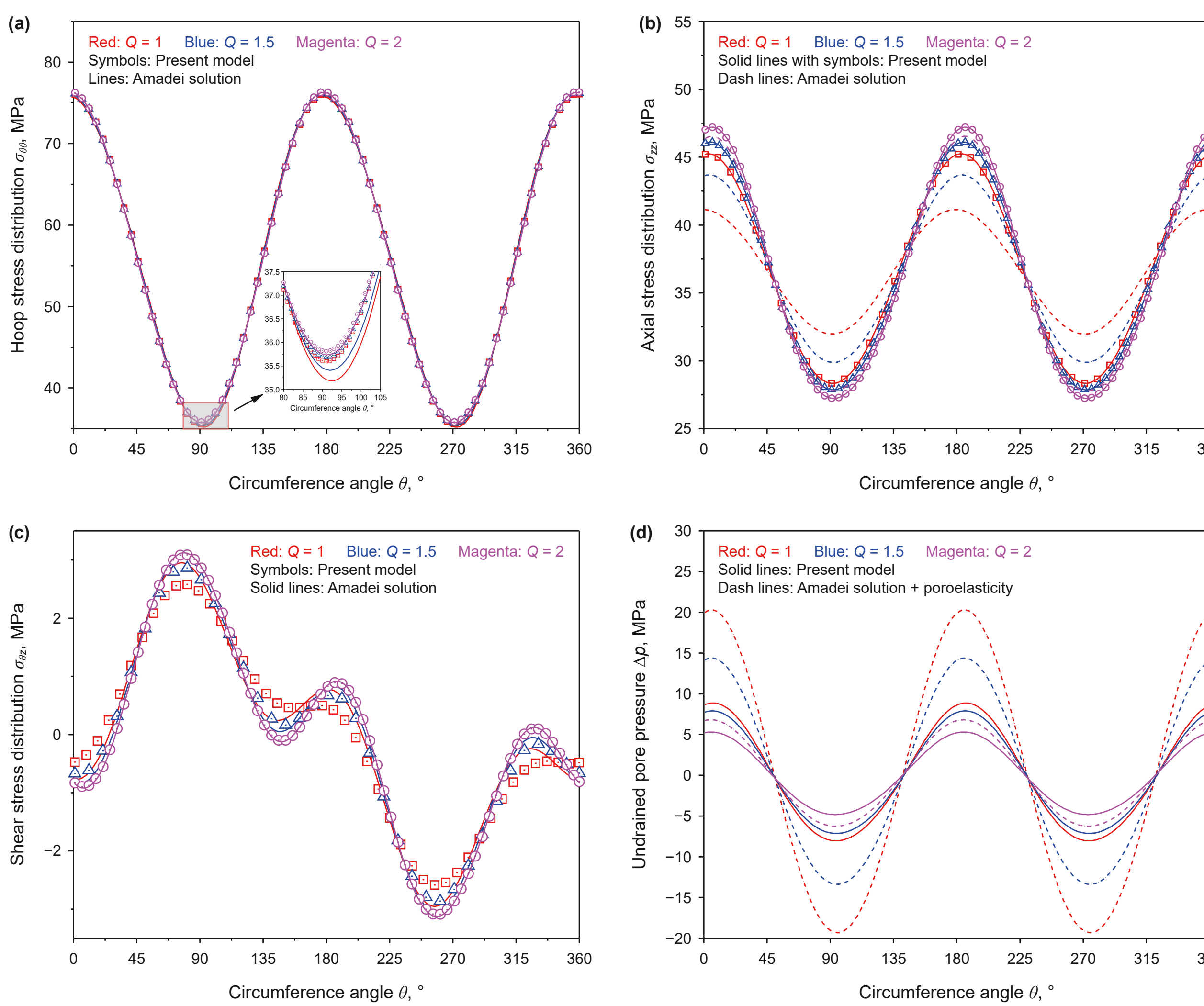

Fig. 7. Influence of Poisson's ratio anisotropy on the poroelastic response ($P = 0.7$, $P_w = 25$ MPa).

As illustrated in Fig. 6(d), the distribution range of undrained pore pressure markedly increases as elastic modulus anisotropy rises ($P\rightarrow 0$). This observation indicates that the undrained pore pressure response is more pronounced under conditions of strong elastic modulus anisotropy ($P = 0.4$). Additionally, circumferential angles corresponding to peak values vary considerably with P. Furthermore, predictions using drained Amadei stress solution significantly overestimate the undrained pore pressure response compared to the present model, further highlighting the necessity of an anisotropic undrained constitutive framework for accurate analysis of anisotropic Skempton effect.

(2) **Poisson's ratio anisotropy**

Fig. 7 illustrates the wellbore stress and pore pressure distributions on the borehole wall, comparing the present model with Amadei solution under varying Poisson's ratio anisotropy Q. In general, the profiles of all stress components exhibit insignificant variation in the present model in Fig. 7(a) and (c). In contrast, substantial fluctuations of axial stress σ_{zz} for varying Poisson's ratio anisotropy are observed in Amadei solution in Fig. 7(b), thereby underscoring the distinctions between the undrained and drained solutions. Concerning the undrained pore pressure response shown in Fig. 7(d), distribution range of the undrained pore pressure declines with increasing Poisson's ratio anisotropy, suggesting a weakening undrained pore pressure response with high Poisson's ratio anisotropy, differing from enhancing effect of elastic modulus anisotropy.

3.3.2. Influence of wellbore pressure

Fig. 8 presents the wellbore stress and pore pressure distributions across varying wellbore pressures. Generally, the hoop stress $\sigma_{\theta\theta}$ distributions under undrained and drained conditions exhibit minimal differences, as depicted in Fig. 8(a). Conversely, as P_w decreases, discrepancies in the distributions of σ_{zz}, $\sigma_{\theta z}$ between the present and Amadei solutions progressively become more pronounced, as illustrated in Fig. 8(b) and (c). Furthermore, with low P_w (15 MPa), the peak values of σ_{zz} and corresponding circumference angles diverge from those predicted by Amadei solution (Fig. 8(b)), emphasizing the critical need to apply an anisotropic undrained constitutive law. In contrast, distribution range of undrained $\sigma_{\theta z}$ remains relatively stable despite changes in P_w, in contrast to the result predicted by Amadei solution, as depicted in Fig. 8(c).

As illustrated in Fig. 8(d), the asymmetric undrained pore pressure distribution using Amadei stress solution is markedly overestimated, as indicated by dashed lines. When P_w (15 MPa)

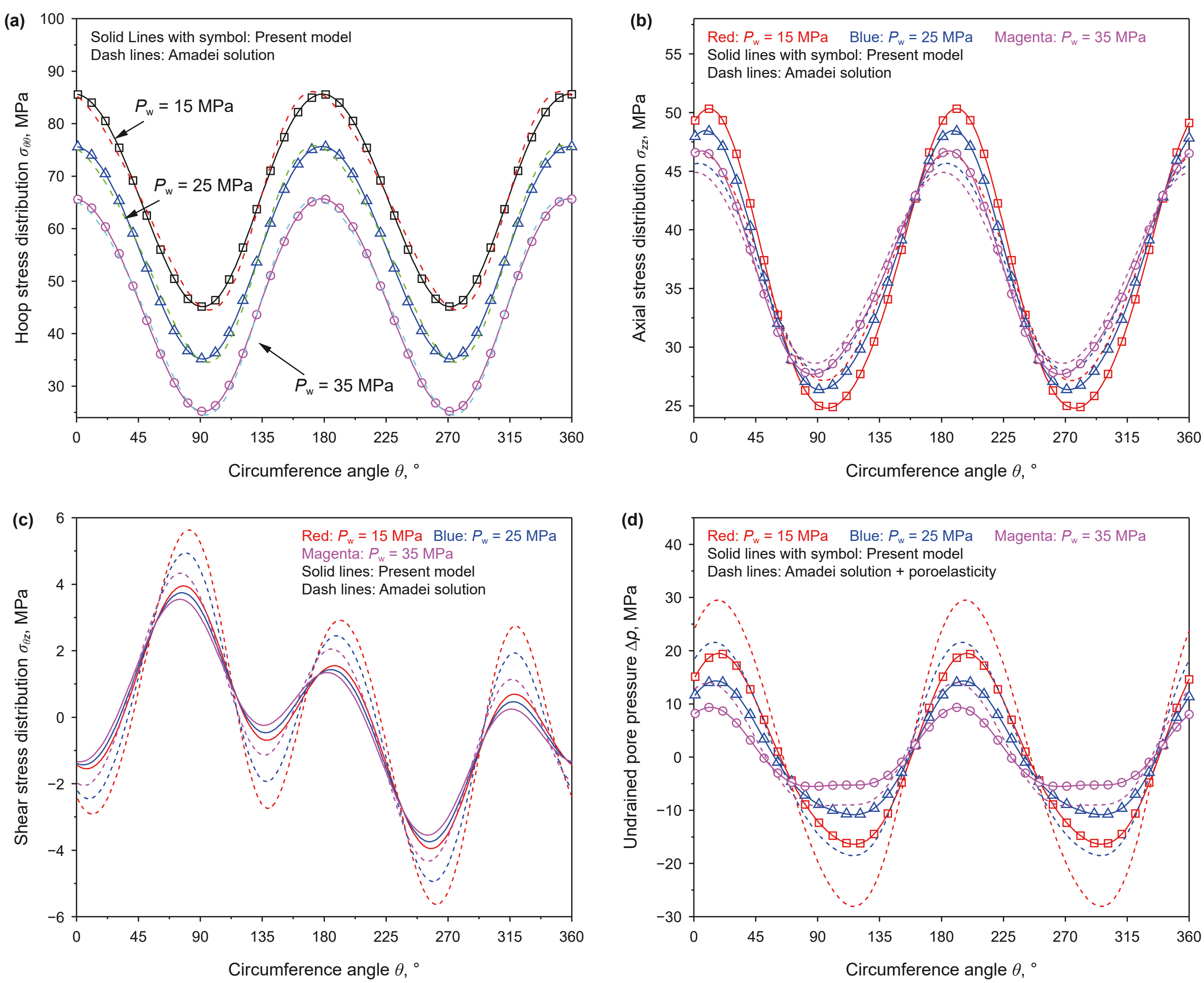

Fig. 8. Non-zero stress distribution under undrained/drained conditions ($P = 0.7$, $Q = 1.5$) with varying wellbore pressure.

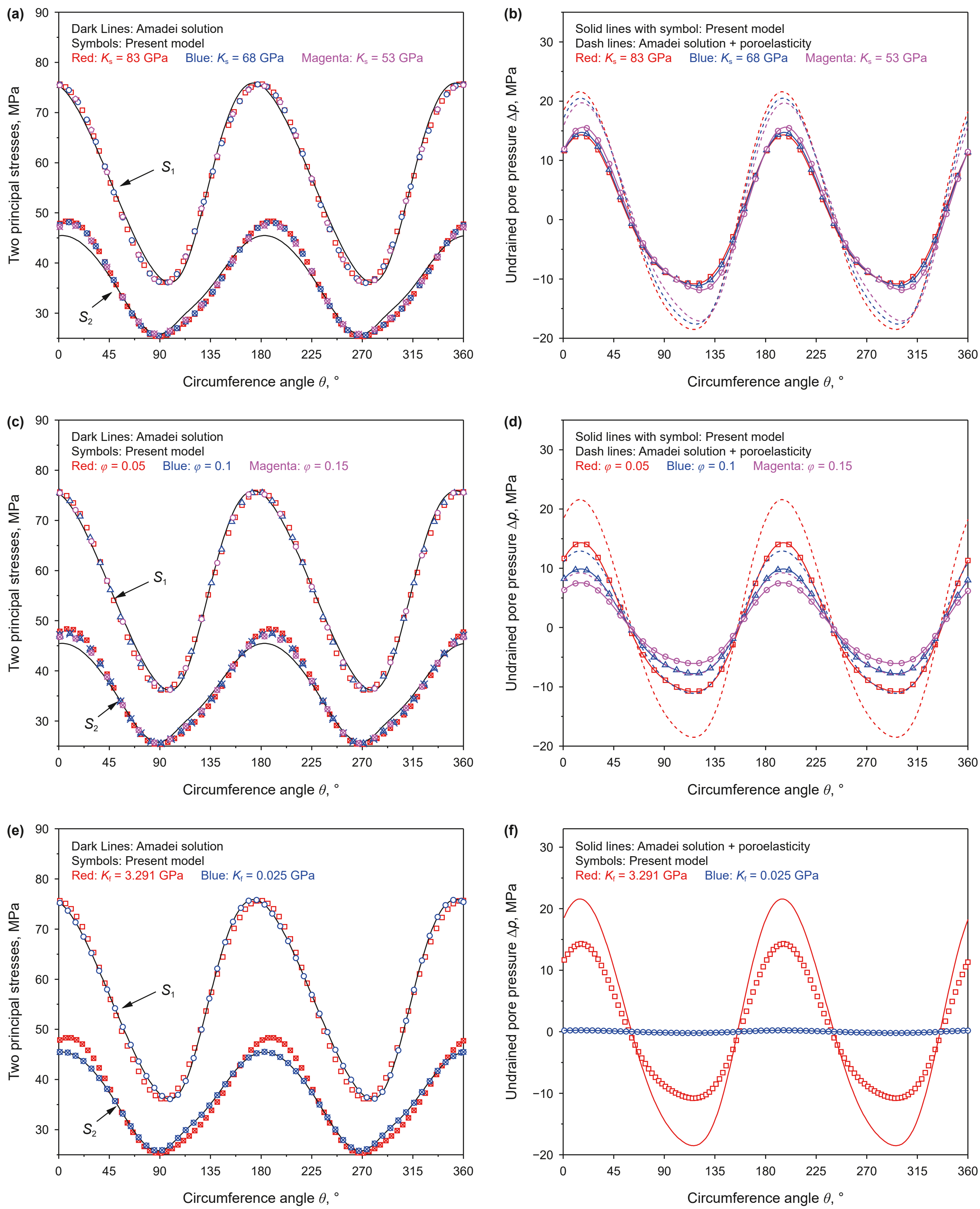

Fig. 9. Profiles of two principal stresses and undrained pore pressure with varying K_s, φ, and K_f.

deviates substantially from the in-situ stress components ($\sigma_{xx}^{b} = 35.4$ MPa, $\sigma_{yy}^{b} = 45.6$ MPa, and $\sigma_{zz}^{b} = 36.6$ MPa), the distribution range of Δp broadens considerably, highlighting the necessity of accounting for the anisotropic undrained poroelastic response, particularly at lower wellbore pressures.

3.3.3. Influence of poroelastic parameters

The difference between the undrained and drained stiffness matrices is attributed to the term $M[\boldsymbol{\alpha}_0]_{6\times1}[\boldsymbol{\alpha}_0]_{6\times1}^{\mathrm{T}}$ in Eq. (9), which depends on the solid grain modulus K_s, porosity φ and fluid modulus K_f as described in Eqs. (4–8). Profiles of the two principal stresses S_1, S_2 and Δp, varying with K_s, φ and K_f, are displayed in Fig. 9. Minor deviations in the profiles of S_1, S_2 with varying K_s and φ are observed between the undrained and drained conditions, as illustrated in Fig. 9(a) and (c). Conversely, a more pronounced Δp is evident with lower φ in Fig. 9(d), slightly inconsistent with findings reported by Li et al. (2025). When the formation is saturated with gas, the fluid modulus is assumed to correspond to the initial pore pressure for an ideal gas. Due to the high compressibility of gas, the deformation of solid skeleton induced by wellbore excavation induces negligible undrained pore pressure variation in Fig. 9(f), which can be explained by smaller Biot modulus M with low fluid modulus K_f in Table 5. Furthermore, the undrained compliance matrix in Eq. (10) changes little from the drained one with smaller M. Therefore, the conventional drained Amadei solution, which inherently assumes zero pore pressure variation, can model the undrained poroelastic response in gas saturated formations in Fig. 9(e) and (f). This observation is consistent with findings for the isotropic case (Gao et al., 2021; Cheng, 2016).

As summarized in Table 5, anisotropic Biot's effective stress coefficients related to normal stress components α_{ii} ($i = x, y, z$) mainly decrease with diminishing K_s, while those related to the shear stress components α_{ij} ($i \neq j$) change little. Biot modulus M exhibits a significant decreasing trend with increasing φ and decreasing K_f, resulting in lower undrained pore pressure variations. Consequently, a more pronounced anisotropic undrained pore pressure response is positively correlated with Biot modulus.

3.3.4. Influence of wellbore trajectory

The wellbore trajectory, characterized by its inclination and azimuth angles, significantly affects the in-situ stress conditions and the compliance matrix under BCS in Eqs. (11–14). For brevity in this analysis, we focus on variations in the inclination angle. Fig. 10 illustrates the profiles of the two principal stresses S_1, S_2 and undrained pore pressure Δp with varying inclination angle β_b. In this section, the wellbore azimuth $\alpha_b = 45°$ and wellbore pressure $P_w = 25$ MPa are held constant. As β_b changes, the locations or magnitudes of peak stresses and pore pressures both shift significantly compared to the drained scenario. Specifically, when the borehole is oriented horizontally with $\beta_b = 90°$, the minimum value of S_1 is observed to be 3.4 MPa lower than that in the drained condition (magenta dashed lines with symbols in Fig. 10(a)). The profile of the undrained pore pressure also changes significantly with varying β_b, as depicted in Fig. 10(b).

This highlights that wellbore trajectory is a critical parameter in undrained poroelastic response, as varying wellbore trajectory can induce significantly different undrained stress and pore pressure response.

4. Short-term collapse pressure determination

To comprehensively analyze the short-term collapse pressure accounting for the fully anisotropic undrained poroelastic response, a detailed parameter investigation was conducted. The input parameters are listed in Table 1. By combining the principal

Table 5
Anisotropic Biot's effective coefficients and Biot modulus with varying poroelastic parameters.

Poroelastic parameters		Unit	α_{xx}	α_{yy}	α_{zz}	α_{yz}	α_{xz}	α_{xy}	M, GPa
K_s	83	GPa	0.569	0.618	0.602	0.057	−0.028	−0.033	45.9
	68		0.474	0.534	0.514	0.069	−0.035	−0.040	45.6
	53		0.325	0.402	0.376	0.089	−0.044	−0.051	47.2
φ	0.05	-	0.569	0.618	0.602	0.057	−0.028	−0.033	45.9
	0.1								27.5
	0.15								19.6
K_f	3.291	GPa							45.9
	0.025								0.50

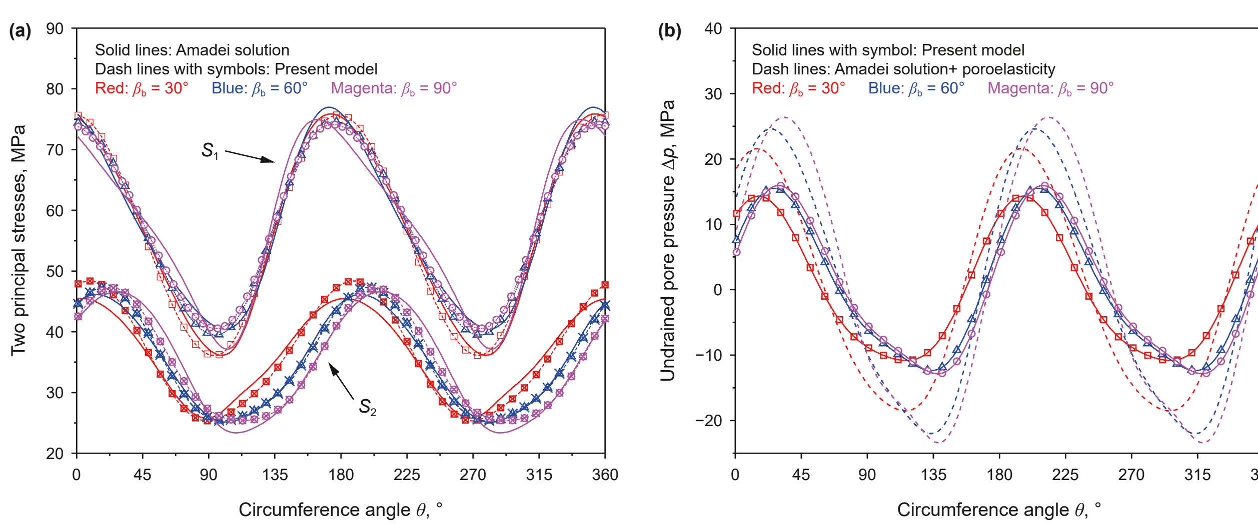

Fig. 10. Profiles of the two principal stresses and undrained pore pressure response with varying wellbore inclination angle.

Biot's effective stresses with failure criteria for both BP and matrix, the collapse pressure can be determined. A critical distinction arises when comparing the present model with conventional approaches. Specifically, the conventional anisotropic model proposed by Liu et al. (2016) assumes a constant pore pressure equal to the initial pore pressure, thereby neglecting the undrained effects on short-term wellbore stability. In addition, the combined "Amadei solution + poroelasticity" approach enhances the representation of the undrained poroelastic response in Figs. 5–10 significantly impacting wellbore stability prediction.

4.1. Collapse pressure analysis using various models

4.1.1. Comparative profiles of the three effective principal stresses: present versus existing models

To further elucidate the mechanisms of wellbore failure, it is essential to analyze the three Biot's effective principal stresses distributions. Fig. 11 illustrates the discrepancies between the three principal stresses S_i (i = 1–3) and their corresponding effective ones $S_i^{\mathrm{eff}}(i = 1-3)$. Due to the anisotropic nature of Biot's effective stress coefficients, as detailed in Table 5, the peak point angles of $S_i^{\mathrm{eff}}(i = 1-3)$ do not coincide with those of the respective effective ones, a behavior absent under isotropic conditions. Moreover, anisotropic Biot's effective stress coefficients vary with alterations in the wellbore trajectory, as outlined in Eqs. (11–14) and Table 3, thereby affecting the distribution of effective stresses and the subsequent prediction of wellbore stability.

Fig. 12 presents the profiles of three Biot's effective principal stresses $S_i^{\mathrm{eff}}(i = 1-3)$ derived from different models with $\alpha_{\mathrm{b}} = 45°$ and $\beta_{\mathrm{b}} = 30°$. The distinct variations in the effective stress profiles arise from differences in stress and pore pressure distributions inherent to each model. The proposed model produces a moderate range of the effective principal stresses compared to the models proposed by Liu et al. (2016) and the combined "Amadei solution + poroelasticity" approach. Additionally, it is observed that the peak values of $S_i^{\mathrm{eff}}(i = 1-3)$ do not occur at identical circumference angles, contrasting with observations under isotropic conditions.

4.1.2. Determination of failure potential and collapse pressure

Failure potentials of both matrix and BP under varying wellbore pressures, as predicted by different models, are illustrated in Fig. 13. In general, the failure potential associated with BP (solid lines) exceeds that of the intact matrix (dashed lines). Consequently, the collapse pressure is identified at the intersection point where the failure potential curve of BP meets the criterion with $F_{\mathrm{bp}} = 0$ in Eq. (29). In this investigation, the collapse pressures estimated by the present model (Model I), Liu et al.'s (2016) Model II, and Model III employing the combined "Amadei solution + poroelasticity" approach show a decreasing trend: $P_{\mathrm{c}}^{\mathrm{III}} > P_{\mathrm{c}}^{\mathrm{I}} > P_{\mathrm{c}}^{\mathrm{II}}$, respectively. Furthermore, as the wellbore pressure increases beyond a certain threshold called as upper collapse pressure, shear failure may occur in both BP or intact matrix, as noted in previous studies (Liu et al., 2016; Ding et al., 2021; Liu et al., 2022; Lu et al., 2025). This study focuses on the allowable lower collapse pressure maintaining wellbore stability, since drilling speed can be elevated under lower wellbore pressure conditions.

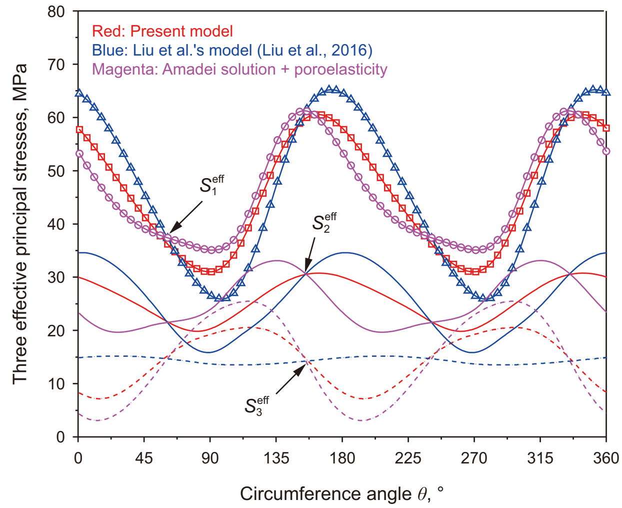

Fig. 12. Profiles of three effective principal stresses with different models.

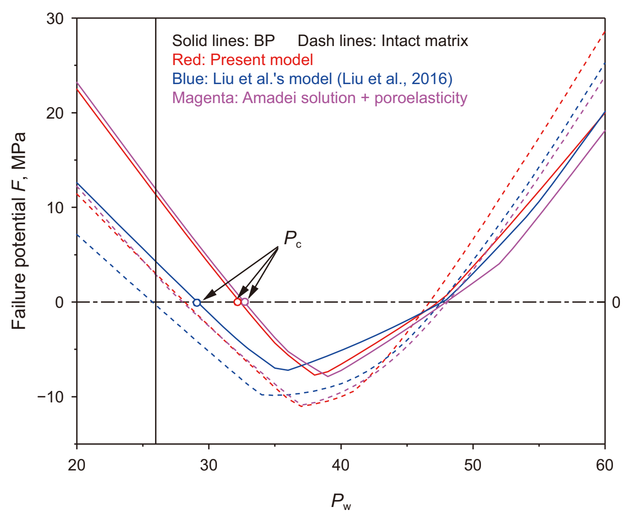

Fig. 13. Failure potential with varying wellbore pressure with $\alpha_{\mathrm{b}} = 45°$, $\beta_{\mathrm{b}} = 30°$.

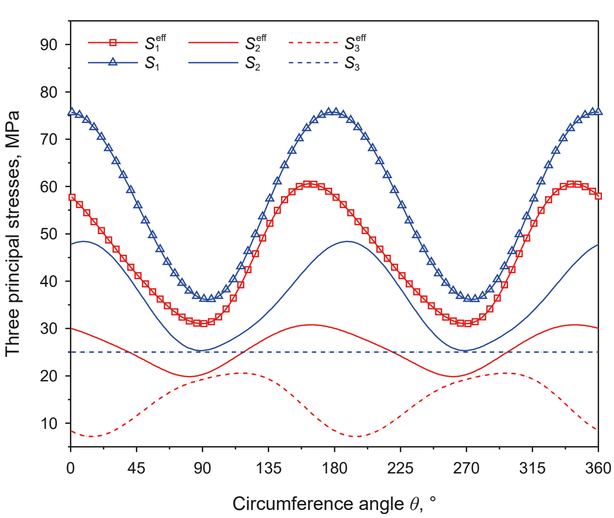

Fig. 11. Difference of three principal stresses and the effective ones.

4.2. Short-term collapse pressure analysis

4.2.1. Comparative evaluation of collapse pressure across different wellbore trajectories

Fig. 14 presents polar plots of collapse pressure across various models, utilizing the specified parameters under a strike-slip

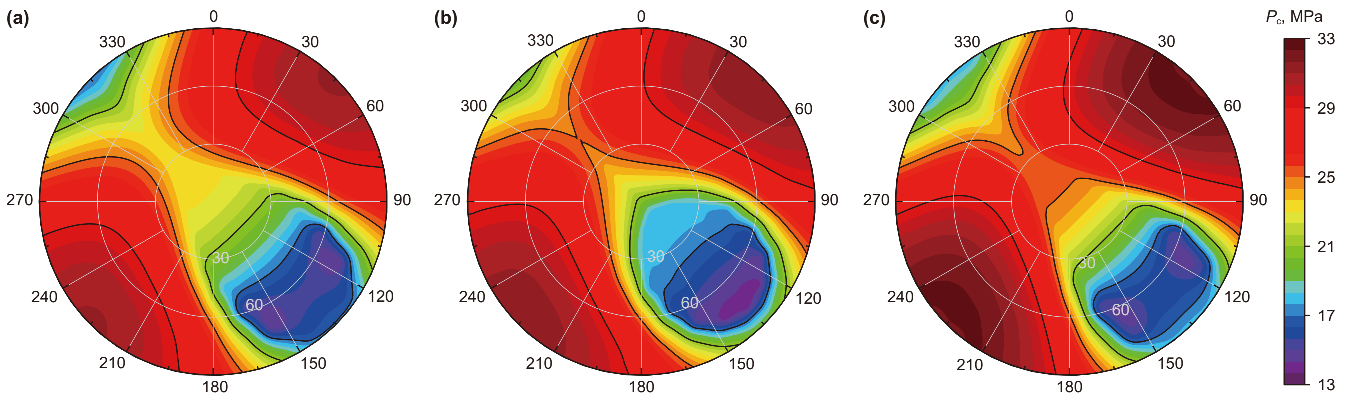

Fig. 14. Polar plots of collapse pressure in different models: (**a**) present Model I, (**b**) Model II by Liu et al. (2016) and (**c**) Model III using “Amadei solution + poroelasticity” approach ($P = 0.4$, $Q = 1.5$).

faulting stress regime in Table 1. The concentric circles denote increasing wellbore inclination, with the outermost circle representing horizontal wells and the centre corresponding to vertical wells. The azimuth angles are indicated by the numerical values around the outer circumference. This polar plot demonstrates that the collapse pressure is dependent on the wellbore trajectory, governed by the Biot's effective stress distributions and anisotropic mechanical strengths. Variations in the profiles of the three effective principal stresses across the models, as depicted in Fig. 12, result in distinct polar patterns of collapse pressure.

Collapse pressures are relatively low when the borehole is oriented nearly parallel to the maximum horizontal principal stress direction and dip direction with $\alpha_b = 135°/315°$. Furthermore, the collapse pressures with dip direction ($\alpha_b = 315°$) exceed those with $\alpha_b = 135°$, indicating that it is safer to drill with a well trajectory perpendicular to the BP. This result is in accordance with on-site observations by Last (1996). Higher collapse pressures are observed when drilling aligns closely with the minimum horizontal principal stress direction with $\alpha_b = 45°/225°$. Notably, the minimum collapse pressures in Models I and III occur at wellbore azimuths offset from the maximum horizontal principal stress direction, a phenomenon attributed to anisotropic poroelastic response and six non-zero Biot's effective stress coefficients, which contrasts with findings in Model II reported by Liu et al. (2016).

Table 6
Peak collapse pressures and corresponding wellbore trajectories.

Models	Minimum P_c, MPa	Wellbore trajectory (α_b, β_b), °	Maximum P_c, MPa	Wellbore trajectory (α_b, β_b), °
Present Model I	14.14	111/159, 66	31.91	42/228,89
Model II: Liu et al. (2016)	13.85	135, 72–74	31.55	66/204, 86
Model III: Amadei solution + poroelasticity	14.65	115/155, 65	32.7	45/225, 84

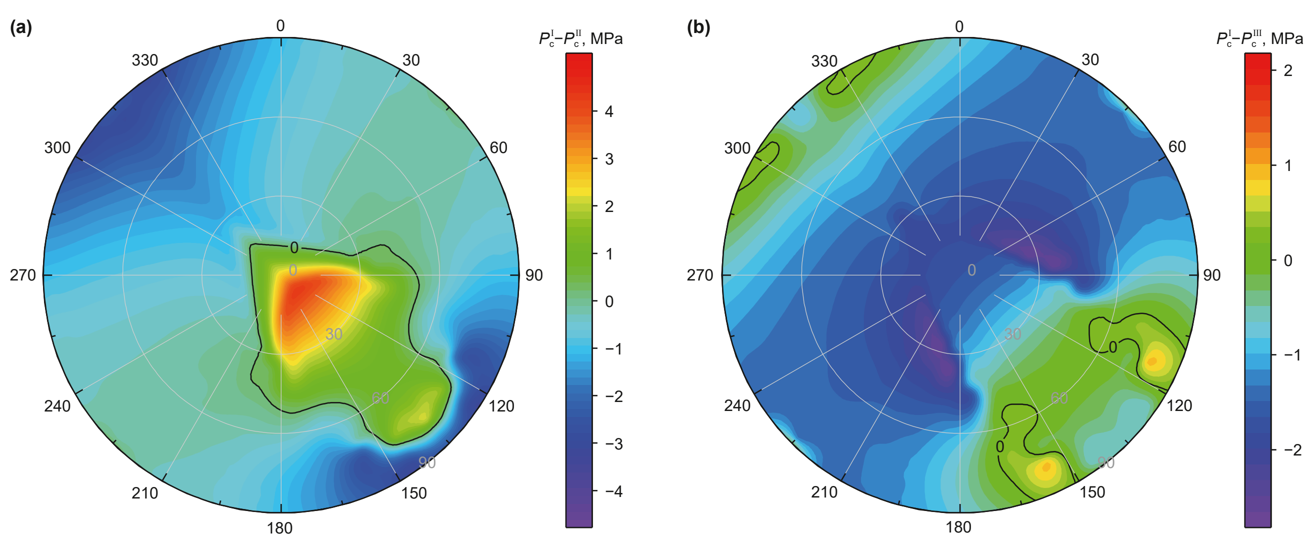

Fig. 15. Polar plot of collapse pressure difference between the present Model I and the other two models: (**a**) Model II by Liu et al. (2016); (**b**) Model III using “Amadei solution + poroelasticity” approach.

Table 6 summarizes the minimum and maximum collapse pressures alongside their corresponding wellbore trajectories, determined using a 1° interval for both inclination and azimuth angles. The peak collapse pressures and their associated trajectories differ among the three models. Specifically, Model II records the lowest minimum collapse pressure, whereas Model III exhibits the highest. For maximum collapse pressures, Model II and Model III represent the minimum and maximum values, respectively. Additionally, the wellbore trajectories corresponding to these extreme values are closely aligned in Models I and III but differ markedly from those in Model II. These results underscore the necessity of incorporating an appropriate anisotropic undrained poroelastic response to achieve a more precise characterization of collapse pressure distributions.

To elucidate the distinctions among the three models, polar plots depicting the differences in collapse pressure between the proposed Model I and the other two models are presented in Fig. 15. Relative to Model I, Models II and III either overestimate or underestimate the collapse pressure depending on the wellbore trajectory, highlighting the complexity inherent in the anisotropic undrained poroelastic response. Specifically, Model II substantially underestimates the collapse pressure ($P_c^{\mathrm{I}} > P_c^{\mathrm{II}}$) near the directions of the maximum horizontal principal stress $\alpha_b = 135°$, while it overestimates the collapse pressure in other wellbore trajectories. In contrast, Model III predominantly overestimates the collapse pressure compared to Model I ($P_c^{\mathrm{I}} < P_c^{\mathrm{III}}$), except for certain specific wellbore trajectories with $\alpha_b \approx 105°/165°$, $\beta_b > 60°$. Therefore, the present Model I is recommended for accurately accounting for the anisotropic undrained effects in addressing short-term wellbore stability challenges.

4.2.2. Influence of elastic property anisotropy

Fig. 16 demonstrates the influence of elastic property anisotropy on the polar plots of collapse pressure with varying P and Q. A comparison of the contour lines in Fig. 16(a–c), reveals that both the minimum and maximum collapse pressure values increase with rising P, suggesting that a reduction in the elastic modulus anisotropy leads to an overall increase in P_c. Furthermore, the zone characterized by low collapse pressure ($P_c \le 18$ MPa) notably

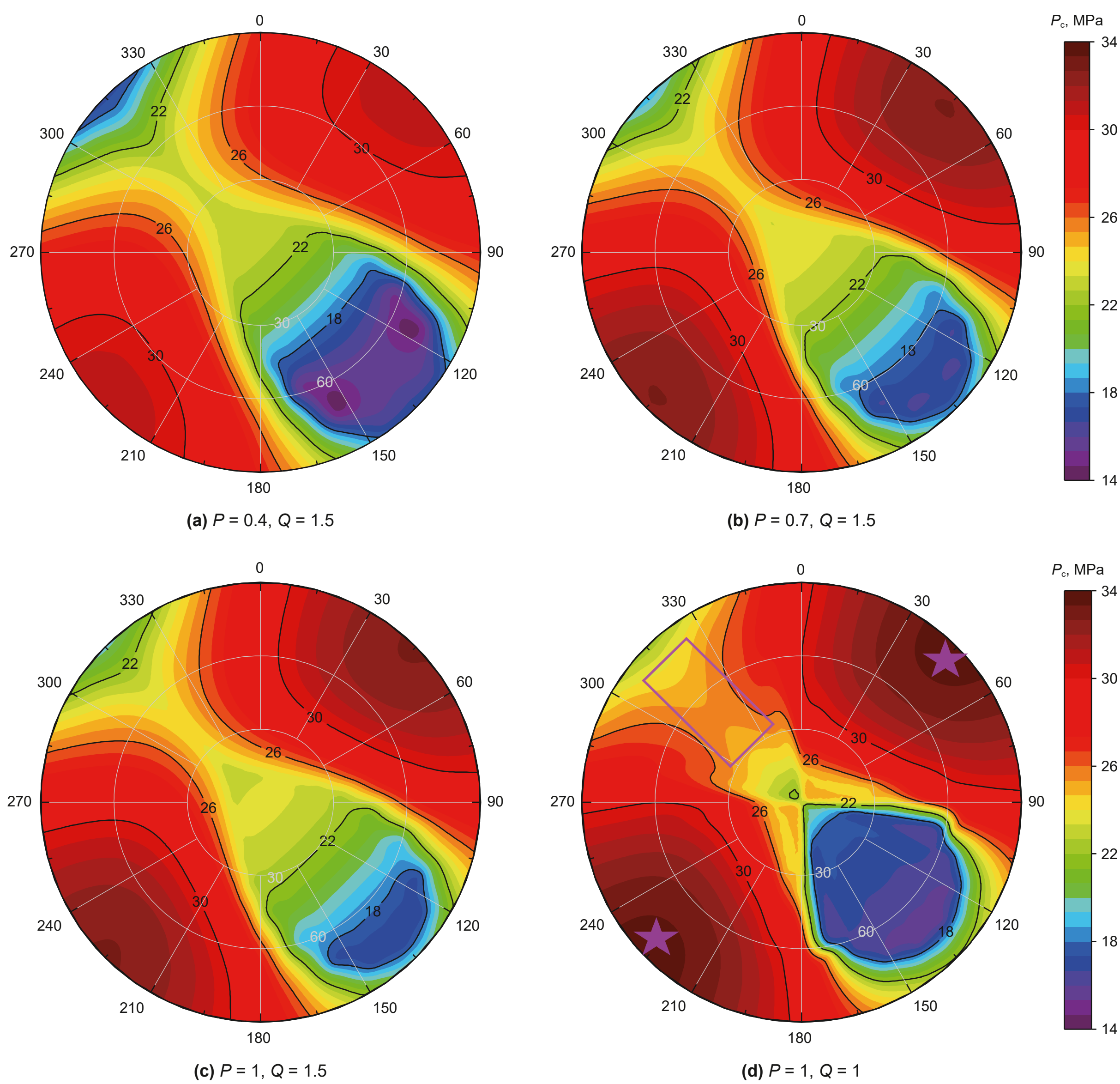

Fig. 16. Effect of elastic property anisotropy on the polar plots of collapse pressure.

diminishes with increasing P, indicating that decreasing elastic modulus anisotropy exacerbates wellbore stability challenges near the direction of maximum horizontal principal stress with $\alpha_b \in (105°,165°)$. The increasing minimum value of P_c and decreasing zone of low collapse pressure, underscore the complexity inherent in anisotropic short-term wellbore stability issue, which should be studied with specified wellbore trajectory.

Regarding the impact of Poisson's ratio anisotropy Q on collapse pressure, a broader range of P_c is observed under isotropic conditions with $P = Q = 1$, as evidenced by Fig. 16(c) and (d). Lower $P_c \leq 15$ MPa can be attained, and a more pronounced peak is observed near the region corresponding to $\alpha_b = 45°/225°$, $\beta_b \approx 90°$, marked by two pentagrams in Fig. 16(d). The isotropic case also exhibits a larger region with $P_c < 18$ MPa, while the region with $18 < P_c < 22$ MPa becomes smaller, compared to the case with $P = 1$ and $Q = 1.5$. An increase in P_c is noted near the region with $\alpha_b = 315°$, indicated by a rectangle in Fig. 16(d). These findings highlight that Poisson's ratio anisotropy also exerts a non-negligible effect on short-term collapse pressure, consistent with the observations presented in Fig. 7.

5. Conclusion and discussion

This study derives a fully anisotropic undrained wellbore stress solution for an arbitrarily inclined borehole in transversely isotropic formations, encompassing all stress components and pore pressure variations. The principal findings are as follows.

(1) When the borehole axis is neither perpendicular nor parallel to the isotropic plane, the fully anisotropic borehole problem is governed by wellbore trajectory, leading to six non-zero Biot's effective stress coefficients rather than the conventional two. The resulting undrained stress distributions notably differ from classical drained Amadei solution, particularly in terms of axial and shear stress components. Increasing elastic modulus anisotropy, decreasing Poisson's ratio anisotropy and wellbore pressure, cause a more significant deviation of the undrained stress solution from the drained Amadei solution.

(2) The undrained pore pressure response exhibits an asymmetrical distribution. This asymmetry is driven by the interplay between wellbore trajectory and poroelastic anisotropy, distinguishing it markedly from the isotropic case. The complex interplay of fluid–solid and shear-tension couplings, alongside six non-zero Biot's effective stress coefficients, critically affects the anisotropic undrained pore pressure response. Furthermore, due to six non-zero Biot's effective stress coefficients, the principal stresses do not coincide with the corresponding effective ones at same circumference angles, a phenomenon absent in isotropic case.

(3) Polar plots of collapse pressure indicate that the optimal drilling direction may diverge from the orientation of the horizontal principal stress due to the anisotropic undrained pore pressure response and the influence of six non-zero anisotropic Biot's effective stress coefficients. This model offers improved accuracy compared to previous approaches: the “Amadei solution with poroelasticity” generally overestimates collapse pressure, and models neglecting pore pressure variations (e.g., Liu et al., 2016) can either underestimate or overestimate it, depending on the wellbore trajectory.

Thus, the proposed fully anisotropic undrained poroelastic solution provides a more accurate foundation for short-term wellbore stability evaluation of arbitrarily inclined boreholes in low-permeability transversely isotropic formations. This advancement has direct practical implications for optimized mud weight design and drilling trajectory planning, enabling more reliable prevention of borehole collapse during early-time operations. Previous analytical studies (Rice and Cleary, 1976; Gao et al., 2016, 2024, 2025) have addressed fluid permeation in isotropic formations through so-called short-time solution, which combine the undrained poroelastic solution and poroelastic stress induced by fluid permeation. In such frameworks, the undrained poroelastic solution serves as the mechanical baseline. The derivation of an analytical short-time solution for inclined boreholes that incorporates fully anisotropic fluid flow remains a significant analytical challenge.

CRediT authorship contribution statement

Wen-Da Li: Writing – original draft, Validation, Methodology, Formal analysis, Conceptualization. **Ya-Yun Zhang:** Writing – original draft, Formal analysis. **Ming-Ming Zhang:** Validation, Formal analysis. **Yan Jin:** Supervision, Funding acquisition, Conceptualization. **Yun-Hu Lu:** Supervision, Formal analysis. **Yang Xia:** Validation, Formal analysis. **Shi-Ming Wei:** Formal analysis.

Data availability

The data that support the findings of this study are available from the corresponding author upon reasonable request.

Declaration of interests

The authors declare that they have no known competing financial interests or personal relationships that could have appeared to influence the work reported in this paper.

Acknowledgements

This work is funded by the National Natural Science Foundation of China (Nos. U24B200085, 52404034, and 52374021).

Appendix A. Far-field in-situ stress transformation

The far-field stress distribution should be transformed from the principal stress coordinate system (PCS) to the borehole coordinate system (BCS), which is given as (Liu et al., 2016):

$$\boldsymbol{\sigma}_{\mathrm{b}} = \boldsymbol{R}_2 \times \boldsymbol{R}_1^{\mathrm{T}} \times \boldsymbol{\sigma}_{\mathrm{p}} \times \boldsymbol{R}_1 \times \boldsymbol{R}_2^{\mathrm{T}} = \left\{ \begin{matrix} \sigma_{xx}^{\mathrm{b}} & \tau_{xy}^{\mathrm{b}} & \tau_{xz}^{\mathrm{b}} \\ \tau_{xy}^{\mathrm{b}} & \sigma_{yy}^{\mathrm{b}} & \tau_{yz}^{\mathrm{b}} \\ \tau_{xz}^{\mathrm{b}} & \tau_{yz}^{\mathrm{b}} & \sigma_{zz}^{\mathrm{b}} \end{matrix} \right\} \tag{A-1}$$

with

$$\boldsymbol{\sigma}_{\mathrm{p}}=\begin{Bmatrix}\sigma_{\mathrm{H}} & 0 & 0\\ 0 & \sigma_{\mathrm{h}} & 0\\ 0 & 0 & \sigma_{\mathrm{v}}\end{Bmatrix};\quad \boldsymbol{R}_1=\begin{Bmatrix}\cos\alpha_{\mathrm{s}}\cos\beta_{\mathrm{s}} & \sin\alpha_{\mathrm{s}}\cos\beta_{\mathrm{s}} & \sin\beta_{\mathrm{s}}\\ -\sin\alpha_{\mathrm{s}} & \cos\alpha_{\mathrm{s}} & 0\\ -\cos\alpha_{\mathrm{s}}\sin\beta_{\mathrm{s}} & -\sin\alpha_{\mathrm{s}}\sin\beta_{\mathrm{s}} & \cos\beta_{\mathrm{s}}\end{Bmatrix} \tag{A-2}$$

where $\boldsymbol{\sigma}_{\mathrm{p}}$, $\boldsymbol{\sigma}_{\mathrm{b}}$ are the initial in-situ stress matrix under PCS and BCS, respectively.

Appendix B. Drained and undrained poroelastic response of an inclined borehole in isotropic formations

The analytical solution of undrained poroelastic response on the borehole wall in the isotropic formation is rewritten in following. The interesting reader can refer to the previous contributions (Chen et al., 2023; Gao et al., 2024; Lu et al., 2025). Taking compressive stress as positive, the drained and undrained poroelastic solution on/near the borehole wall are given as (Gao et al., 2024)

$$\sigma_{\theta\theta}=\sigma_{xx}^{\mathrm{b}}+\sigma_{yy}^{\mathrm{b}}-2\left(\sigma_{xx}^{\mathrm{b}}-\sigma_{yy}^{\mathrm{b}}\right)\cos2\theta-4\tau_{xy}^{\mathrm{b}}\sin2\theta-P_{\mathrm{w}} \tag{B-1}$$

$$\begin{cases}\sigma_z^{\mathrm{d}}=\sigma_{zz}^{\mathrm{b}}-2\nu\sqrt{\left(\dfrac{\sigma_{xx}^{\mathrm{b}}-\sigma_{yy}^{\mathrm{b}}}{2}\right)^2+\tau_{xy}^{\mathrm{b}}}\cos2(\theta-\theta_r)\\ \sigma_z^{\mathrm{u}}=\sigma_{zz}^{\mathrm{b}}-2\nu_{\mathrm{u}}\sqrt{\left(\dfrac{\sigma_{xx}^{\mathrm{b}}-\sigma_{yy}^{\mathrm{b}}}{2}\right)^2+\tau_{xy}^{\mathrm{b}}}\cos2(\theta-\theta_r)\end{cases} \tag{B-2}$$

$$\tau_{\theta z}=2\tau_{yz}^{\mathrm{b}}\cos\theta-2\tau_{xz}^{\mathrm{b}}\sin\theta \tag{B-3}$$

$$\begin{aligned}\Delta p&=\frac{2\alpha M}{\lambda+\alpha^2M+G}\sqrt{\left(\frac{\sigma_{xx}^{\mathrm{b}}-\sigma_{yy}^{\mathrm{b}}}{2}\right)^2+\tau_{xy}^{\mathrm{b}}}\cos2(\theta-\theta_r)\\ &=\frac{4B}{3}(1+\nu_{\mathrm{u}})\sqrt{\left(\frac{\sigma_{xx}^{\mathrm{b}}-\sigma_{yy}^{\mathrm{b}}}{2}\right)^2+\tau_{xy}^{\mathrm{b}}}\cos2(\theta-\theta_r)\end{aligned} \tag{B-4}$$

with

$$\begin{aligned}&B=\frac{\alpha M}{K+\alpha^2M},\lambda=\frac{2G\nu}{(1-2\nu)},\nu_u=\frac{3\nu+\alpha B(1-2\nu)}{3-\alpha B(1-2\nu)},\\ &\theta_r=\frac{1}{2}\arctan\left(\frac{2\tau_{xy}^{\mathrm{b}}}{\sigma_x^{\mathrm{b}}-\sigma_y^{\mathrm{b}}}\right).\end{aligned} \tag{B-5}$$

Appendix C. Undrained poroelastic response of a horizontal borehole in transversely isotropic formations

The analytical solution of a horizontal borehole in transversely isotropic formations can refer to the previous contributions (Bobet, 2011; Tran et al., 2022; Lu et al., 2025). In this scenario, take tensile stress as positive. When the borehole is drilled along the minimum horizontal principal stress direction, the normal stress and pore pressure distributions can be given as (Lu et al., 2025)

$$\begin{aligned}&\sigma_x^{\mathrm{u}}=\sigma_{\mathrm{H}}+\Delta\sigma_x^{\mathrm{u}}=\sigma_{\mathrm{H}}+2\left[\frac{\mu_{1\mathrm{S}}{}^2\cdot A_{1\mathrm{S}}\cdot C_{1\mathrm{S}}}{C_{1\mathrm{S}}{}^2+D_{1\mathrm{S}}{}^2}+\frac{\mu_{2\mathrm{S}}{}^2\cdot A_{2\mathrm{S}}\cdot C_{2\mathrm{S}}}{C_{2\mathrm{S}}{}^2+D_{2\mathrm{S}}{}^2}\right],\\ &\sigma_y^{\mathrm{u}}=\sigma_{\mathrm{v}}+\Delta\sigma_y^{\mathrm{u}}=\sigma_{\mathrm{v}}-2\left[\frac{A_{1\mathrm{S}}\cdot C_{1\mathrm{S}}}{C_{1\mathrm{S}}{}^2+D_{1\mathrm{S}}{}^2}+\frac{A_{2\mathrm{S}}\cdot C_{2\mathrm{S}}}{C_{2\mathrm{S}}{}^2+D_{2\mathrm{S}}{}^2}\right],\\ &\sigma_z^{\mathrm{u}}=\sigma_{\mathrm{h}}-\left(\nu\Delta\sigma_x^{\mathrm{u}}+\nu'\Delta\sigma_y^{\mathrm{u}}\Big/P+\beta_4\Delta p\right),\\ &\Delta p=-\frac{2}{\beta_3}\left[\left(\beta_2-\beta_1\mu_{1\mathrm{S}}{}^2\right)\frac{A_{1\mathrm{S}}\cdot C_{1\mathrm{S}}}{C_{1\mathrm{S}}{}^2+D_{1\mathrm{S}}{}^2}+\left(\beta_2-\beta_1\mu_{2\mathrm{S}}{}^2\right)\frac{A_{2\mathrm{S}}\cdot C_{2\mathrm{S}}}{C_{2\mathrm{S}}{}^2+D_{2\mathrm{S}}{}^2}\right].\end{aligned} \tag{C-1}$$

with

$$\begin{aligned}&A_{1\mathrm{S}}=\frac{\sigma_{\mathrm{H}}-\mu_{2\mathrm{S}}\sigma_{\mathrm{v}}+(1-\mu_{2\mathrm{S}})P_{\mathrm{w}}}{(\mu_{1\mathrm{S}}-\mu_{2\mathrm{S}})},A_{2\mathrm{S}}=\frac{\sigma_{\mathrm{H}}-\mu_{1\mathrm{S}}\sigma_{\mathrm{v}}+(1-\mu_{1\mathrm{S}})P_{\mathrm{w}}}{(\mu_{2\mathrm{S}}-\mu_{1\mathrm{S}})},\\ &C_{1\mathrm{S}}=(1+\mu_{1\mathrm{S}})\cos2\theta+\mu_{1\mathrm{S}}-1,\ C_{2\mathrm{S}}=(1+\mu_{2\mathrm{S}})\cos2\theta+\mu_{2\mathrm{S}}-1,\\ &D_{1\mathrm{S}}=(1+\mu_{1\mathrm{S}})\sin2\theta,\ D_{2\mathrm{S}}=(1+\mu_{2\mathrm{S}})\sin2\theta,\\ &\beta_1=s_{11}\alpha_{\mathrm{h}}+s_{12}\alpha_{\mathrm{v}},\ \beta_2=s_{12}\alpha_{\mathrm{h}}+s_{22}\alpha_{\mathrm{v}},\\ &\beta_3=\frac{1}{M}+\alpha_{\mathrm{h}}\beta_1+\alpha_{\mathrm{v}}\beta_2,\ \beta_4=(\nu-1)\alpha_{\mathrm{h}}+\nu'\alpha_{\mathrm{v}}\Big/P,\\ &s_{11}=\left(1-\nu^2\right)\Big/E,\ s_{12}=-(1+\nu)\nu'\Big/E',\\ &s_{22}=\left(1-\nu'^2\Big/P\right)\Big/E',\ s_{33}=(E+E'+2\nu'E')\Big/EE'.\end{aligned} \tag{C-2}$$

Two undrained in-plane characteristic roots are used, whose imaginary parts can be obtained analytically as

$$\mu_{1,2\mathrm{S}}=\mathrm{Im}\sqrt{\frac{-(s-2\beta_1\beta_2/\beta_3)\pm\sqrt{(s-2\beta_1\beta_2/\beta_3)^2-4\left(s_{11}-\beta_1{}^2\Big/\beta_3\right)\left(s_{22}-\beta_2{}^2\Big/\beta_3\right)}}{2\left(s_{11}-\beta_1{}^2\Big/\beta_3\right)}} \tag{C-3}$$

with $s=2s_{12}+s_{33}$. Noted that the isotropic plane lies in the x-z plane in Lu et al. (2025), different from that in the present study. In addition, the initial circumference angle in the present model is the lowest point of borehole, while that in Lu et al. (2025) is in the isotropic plane. Thus, the initial angles differ by 90° in two models.

References

Aadnoy, B.S., 1989. Stress around horizontal boreholes drilled in sedimentary rocks. J. Petrol. Sci. Eng. 2 (4), 349–360. https://doi.org/10.1016/0920-4105(89)90009-0.

Abousleiman, Y., Cui, L., 1998. Poroelastic solutions in transversely isotropic media for wellbore and cylinder. Int. J. Solids Struct. 35 (34–35), 4905–4929. https://doi.org/10.1016/S0020-7683(98)00101-2.

Abousleiman, Y.N., Ekbote, S., 2005. Solutions for the inclined borehole in a thermoporoelastic transversely isotropic medium. J. App. Mech. 72 (1), 102–114. https://doi.org/10.1115/1.1825433.
Al-Ajmi, A.M., Zimmerman, R.W., 2005. Relation between the Mogi and the Coulomb failure criteria. Int. J. Rock Mech. Min. Sci. 42 (3), 431–439. https://doi.org/10.1016/j.ijrmms.2004.11.004.
Amadei, B., 1983. Rock Anisotropy and the Theory of Stress Measurements. Springer Science and Business Media, Berlin. https://doi.org/10.1007/978-3-642-82040-3.
Asaka, M., Holt, R.M., 2021. Anisotropic wellbore stability analysis: impact on failure prediction. Rock Mech. Rock Eng. 54 (2), 583–605. https://doi.org/10.1007/s00603-020-02283-0.
Biot, M.A., 1941. General theory of three-dimensional consolidation. J. Appl. Phys. 12 (2), 155–164. https://doi.org/10.1063/1.1712886.
Bobet, A., 2011. Lined circular tunnels in elastic transversely anisotropic rock at depth. Rock Mech. Rock Eng. 44 (2), 149–167. https://doi.org/10.1007/s00603-010-0118-1.
Chen, S.L., Han, Y.H., Abousleiman, Y.N., 2023. Engineering charts development for poroelastic stress analysis of horizontal/inclined borehole and its application for breakdown pressure prediction. SPE J. 28 (3), 1349–1368. https://doi.org/10.2118/214291-pa.
Cheng, A.H.-D., 1997. Material coefficients of anisotropic poroelasticity. Int. J. Rock Mech. Min. Sci. 34 (2), 199–205. https://doi.org/10.1016/s0148-9062(96)00055-1.
Cheng, A.H.-D., 2016. Poroelasticity. Springer International Publishing, Switzerland. https://doi.org/10.1007/978-3-319-25202-5.
Cheng, W., Jiang, G., Li, X., et al., 2019. A porochemothermoelastic coupling model for continental shale wellbore stability and a case analysis. J. Petrol. Sci. Eng. 182, 106265. https://doi.org/10.1016/j.petrol.2019.106265.
Cui, L., Ekbote, S., Abousleiman, Y., et al., 1998. Borehole stability analyses in fluid saturated formations with impermeable walls. Int. J. Rock Mech. Min. Sci. Abstr. 35 (4–5), 582–583. https://doi.org/10.1016/s0148-9062(98)00077-1.
Detournay, E., Cheng, A.H.-D., 1988. Poroelastic response of a borehole in a non-hydrostatic stress field. Int. J. Rock Mech. Mining Sci. Geomech. 25 (3), 171–182. https://doi.org/10.1016/0148-9062(88)92299-1.
Ding, L., Wang, Z., Lv, J., et al., 2021. New methodology to determine the upper limit of safe borehole pressure window: Considering compressive failure of rocks while drilling in anisotropic shale formations. J. Nat. Gas Sci. Eng. 96, 104299. https://doi.org/10.1016/j.jngse.2021.104299.
Duda, M.I., Bakk, A., Holt, R.M., et al., 2023. Anisotropic poroelastic modelling of depletion-induced pore pressure changes in Valhall overburden. Rock Mech. Rock Eng. 56 (4), 3115–3137. https://doi.org/10.1007/s00603-022-03192-0.
Fan, Z., Song, X., Wang, D., et al., 2025. Poroelastic solutions of a semipermeable borehole under nonhydrostatic in situ stresses within transversely isotropic media. Int. J. GeoMech. 25 (2), 04024342. https://doi.org/10.1061/ijgnai.gmeng-10261.
Fang, X., 2018. A revisit to the Lekhnitskii-Amadei solution for borehole stress calculation in tilted transversely isotropic media. Int. J. Rock Mech. Mining Sci. 104, 113–118. https://doi.org/10.1016/j.ijrmms.2018.02.001.
Fjar, E., Holt, R.M., Horsrud, P., et al., 2008. Petroleum Related Rock Mechanics. Elsevier Science. https://doi.org/10.1016/s0376-7361(07)x5300-7.
Gaede, O., Karpfinger, F., Jocker, J., et al., 2012. Comparison between analytical and 3D finite element solutions for borehole stresses in anisotropic elastic rock. Int. J. Rock Mech. Min. Sci. 51, 53–63. https://doi.org/10.1016/j.ijrmms.2011.12.010.
Gao, Y., Chen, M., 2020. Numerical modeling on thermoelastoplastic responses of Karamay oil sand reservoir upon steam circulation considering phase change of bitumen. J. Petrol. Sci. Eng. 187, 106745. https://doi.org/10.1016/j.petrol.2019.106745.
Gao, Y., Liu, Z., Zhuang, Z., et al., 2016. Cylindrical borehole failure in a poroelastic medium. J. App. Mech. 83 (6), 061005. https://doi.org/10.1115/1.4032859.
Gao, J., Lin, H., Wu, B., et al., 2021. Porochemothermoelastic solutions considering fully coupled thermo-hydro-mechanical-chemical processes to analyze the stability of inclined boreholes in chemically active porous media. Comput. Geotech. 134, 104019. https://doi.org/10.1016/j.compgeo.2021.104019.
Gao, J., Chen, F., Zhao, Y., et al., 2024. Quantitative risk analysis and parameter sensitivity evaluation of wellbore instability in poroelastic media considering uncertainty of geomechanical parameters. Comput. Geotech. 170, 106234. https://doi.org/10.1016/j.compgeo.2024.106234.
Gao, J., Bian, G., Lin, H., et al., 2025. Study on wellbore stability considering rock matrix and weak plane of porous shale subjected to polyaxial compression and different time-domain poroelastic solutions. Geoenergy Sci. Eng. 254, 213986. https://doi.org/10.1016/j.geoen.2025.213986.
Gao, Y., Liu, Z., Zhuang, Z., et al., 2017. Cylindrical borehole failure in a transversely isotropic poroelastic medium. J. App. Mech. 84 (11), 111008. https://doi.org/10.1115/1.4037880.
Hou, B., Chen, M., Wang, Z., et al., 2013. Hydraulic fracture initiation theory for a horizontal well in a coal seam. Petro. Sci. 10 (2), 219–225. https://doi.org/10.1007/s12182-013-0270-9.
Kanfar, M.F., Chen, Z., Rahman, S.S., 2015a. Effect of material anisotropy on time-dependent wellbore stability. Int. J. Rock Mech. Min. Sci. 78, 36–45. https://doi.org/10.1016/j.ijrmms.2015.04.024.
Kanfar, M.F., Chen, Z., Rahman, S.S., 2015b. Risk-controlled wellbore stability analysis in anisotropic formations. J. Petrol. Sci. Eng. 134, 214–222. https://doi.org/10.1016/j.petrol.2015.08.004.
Kanj, M., Abousleiman, Y., 2005. Porothermoelastic analyses of anisotropic hollow cylinders with applications. Int. J. Numer. Anal. Met. 29 (2), 103–126. https://doi.org/10.1002/nag.406.
Last, N.C., 1996. Assessing the impact of trajectory on wells drilled in an overthrust region. J. Petrol. Technol. 48 (7), 620–625. https://doi.org/10.2118/30465-ms.
Lee, H., Ong, S.H., Azeemuddin, M., et al., 2012. A wellbore stability model for formations with anisotropic rock strengths. J. Petrol. Sci. Eng. 96–97, 109–119. https://doi.org/10.1016/j.petrol.2012.08.010.
Lekhnitskii, S.G., 1963. Theory of Elasticity of an Anisotropic Elastic Body. Holden-Day, San Francisco. https://doi.org/10.1137/1009023.
Li, W., Zhang, Y., Zhang, M., et al., 2025. Undrained pore pressure response for an inclined well in a transversely isotropic poroelastic formation. In: 59th U.S. Rock Mechanics/Geomechanics Symposium. https://doi.org/10.56952/arma-2025-0459.
Liu, C., Abousleiman, Y.N., 2020. Generalized solution to the anisotropic Mandel's problem. Int. J. Numer. Anal. Met. Geomech. 44 (17), 2283–2303. https://doi.org/10.1002/nag.3128.
Liu, M., Jin, Y., Lu, Y., et al., 2015. Oil-based critical mud weight window analyses in HTHP fractured tight formation. J. Petrol. Sci. Eng. 135, 750–764. https://doi.org/10.1016/j.petrol.2015.10.002.
Liu, M., Jin, Y., Lu, Y., et al., 2016. A wellbore stability model for a deviated well in a transversely isotropic formation considering poroelastic effects. Rock Mech. Rock Eng. 49 (9), 3671–3686. https://doi.org/10.1007/s00603-016-1019-8.
Liu, C., Han, Y., Phan, D.T., et al., 2022. Stress solutions for short-and long-term wellbore stability analysis. J. Nat. Gas Sci. Eng. 105, 104693. https://doi.org/10.1016/j.jngse.2022.104693.
Lu, Y., Li, W., Jin, Y., et al., 2025. Short-and long-term wellbore stability analysis for a horizontal well in a transversely isotropic poroelastic formation. Rock Mech. Rock Eng. 58 (1), 767–786. https://doi.org/10.1007/s00603-024-04183-z.
Ma, T., Liu, Y., Chen, P., et al., 2019. Fracture-initiation pressure prediction for transversely isotropic formations. J. Petrol. Sci. Eng. 176, 821–835. https://doi.org/10.1016/j.petrol.2019.01.090.
Ma, T., Wang, H., Liu, Y., et al., 2022. Fracture-initiation pressure model of inclined wells in transversely isotropic formation with anisotropic tensile strength. Int. J. Rock Mech. Min. Sci. 159, 105235. https://doi.org/10.1016/j.ijrmms.2022.105235.
Nordas, A.N., Cantieni, L., Anagnostou, G., 2025. An analytical solution for the undrained ground response to tunnelling considering the excavation-induced desaturation. J. Rock Mech. Geotech. Eng. 17 (4), 1961–1972. https://doi.org/10.1016/j.jrmge.2024.04.020.
Peng, H., Yue, Y., Luo, X., et al., 2023. Double-porosity poromechanical models for wellbore stability of inclined borehole drilled through the naturally fractured porous rocks. Geoenergy Sci. Eng. 228, 211756. https://doi.org/10.1016/j.geoen.2023.211756.
Qiu, Y., Ma, T., Peng, N., et al., 2023a. Wellbore stability analysis of inclined wells in transversely isotropic formations accounting for hydraulic-mechanical coupling. Geoenergy Sci. Eng. 224, 211615. https://doi.org/10.1016/j.geoen.2023.211615.
Qiu, Y., Ma, T., Liu, J., et al., 2023b. Poroelastic response of inclined wellbore geometry in anisotropic dual-medium/media. Int. J. Rock Mech. Min. Sci. 170, 105560. https://doi.org/10.1016/j.ijrmms.2023.105560.
Qiu, Y., Ma, T., Peng, N., et al., 2024. Fully coupled anisotropic porothermoelasticity modeling for inclined borehole in shale formations. Rock Mech. Rock Eng. 57 (1), 597–619. https://doi.org/10.1007/s00603-023-03569-9.
Raaen, A.M., Larsen, I., Fjar, E., et al., 2019. Pore pressure response in rock: implications of tensorial Skempton B in an anisotropic formation. In: ARMA US Rock Mechanics/Geomechanics Symposium. https://doi.org/10.56952/arma-2022-0672.
Rice, J.R., Cleary, M.P., 1976. Some basic stress diffusion solutions for fluid saturated elastic porous media with compressible constituents. Rev. Geophys. Space Phys. 14 (2), 227–241. https://doi.org/10.1029/rg014i002p00227.
Setiawan, N.B., Zimmerman, R.W., 2018. Wellbore breakout prediction in transversely isotropic rocks using true-triaxial failure criteria. Int. J. Rock Mech. Min. Sci. 112, 313–322. https://doi.org/10.1016/j.ijrmms.2018.10.033.
Soldal, M., Choi, J.C., Skurtveit, E., 2025. Experimental evaluation of predicted undrained pore pressure generation as a function of stress path and material orientation in the draupne shale. Rock Mech. Rock Eng. 58 (6), 6043–6058. https://doi.org/10.1007/s00603-025-04452-5.
Tran, N.H., Do, D.P., Vu, M.N., et al., 2022. Combined effect of anisotropy and uncertainty on the safe mud window of horizontal wellbore drilled in anisotropic saturated rock. Int. J. Rock Mech. Min. Sci. 152, 105061. https://doi.org/10.1016/j.ijrmms.2022.105061.
Vitali, O.P., Celestino, T.B., Bobet, A., 2020. Analytical solution for a deep circular tunnel in anisotropic ground and anisotropic geostatic stresses. Rock Mech. Rock Eng. 53 (9), 3859–3884. https://doi.org/10.1007/s00603-020-02157-5.
Wang, W., Schmitt, D.R., Li, W., 2022. A program to forward model the failure pattern around the wellbore in elastic and strength anisotropic rock formations. Int. J. Rock Mech. Min. Sci. 151, 105035. https://doi.org/10.1016/j.ijrmms.2022.105035.
Zhang, W., Gao, J., Lan, K., et al., 2015. Analysis of borehole collapse and fracture initiation positions and drilling trajectory optimization. J. Petrol. Sci. Eng. 129, 29–39. https://doi.org/10.1016/j.petrol.2014.08.021.
Zhang, M., Fan, X., Zhang, Q., et al., 2021. Parametric sensitivity study of wellbore stability in transversely isotropic medium based on polyaxial strength criteria. J. Petrol. Sci. Eng. 197, 108078. https://doi.org/10.1016/j.petrol.2020.108078.